POTENTIAL ENERGY LANDSCAPE OF PARTICULATE MATTER

by

Kun Wang

A dissertation submitted to the Graduate Faculty in Physics in partial fulfillment of the requirements for the degree of Doctor of Philosophy, The City University of New York

2012

This manuscript has been read and accepted for the
Graduate Faculty in Physics in satisfaction of the
dissertation requirement for the degree of Doctor of Philosophy.

Prof. Hernan Makse

Date

Chair of Examining Committee

Prof. Igor L. Kuskovsky

Date

Executive Officer

Prof. Hernan Makse, City College of New York, CUNY

Prof. Zinoviy Akkerman, Cooper Union (New York)

Prof. Joel Gersten, City College of New York, CUNY

Prof. Ronald Koder, City College of New York, CUNY

Prof. Jeff Morris, City College of New York, CUNY
Supervisory Committee

THE CITY UNIVERSITY OF NEW YORK

Abstract

POTENTIAL ENERGY LANDSCAPE OF PARTICULATE MATTER

by

Kun Wang

Adviser: Professor Hernán A. Makse

The application of concepts from equilibrium statistical mechanics to out of equilibrium systems has a long history of describing diverse systems ranging from glasses to granular materials [1, 2, 3]. These systems are considered "complex" since equilibrium statistics is insufficient in its attempt to describe the system dynamics. An appealing approach for understanding these complex systems is to study the properties of the system's "potential energy landscape" (PEL), described by the $3N$-coordinates of all particles in the multi-dimensional configuration space, or landscape, of the potential energy of the system (N is the number of particles).

For dissipative jammed systems– granular materials or droplets– a key concept introduced by S. Edwards in 1989 is to replace the energy ensemble describing conservative systems by the volume ensemble [3]. However, this approach is not able to describe the jamming critical point (J-point) for deformable particles like emulsions [4, 5, 6], whose geometric configurations are influenced by the applied external stress. Therefore, the volume ensemble requires augmentation by the ensemble of stresses [7, 8, 9, 10]. Just as volume fluctuations in the Edwards ensemble can be described by compactivity, the stress fluctuations give rise to an angoricity, another analogue of temperature in equilibrium systems. In this Thesis, we test the combined volume-stress ensemble for granular matter by comparing the statistical properties of jammed configurations obtained by dynamics with those averaged over the ensemble as a test of ergodicity. Agreement between both methods suggests the idea of “thermalization” at a given angoricity and compactivity. These intensive variables elucidate the thermodynamic order of the jamming phase transition by showing the absence of critical fluctuations above jamming in static observables like pressure and volume. Our results demonstrate the possibility of calculating important observables such as the entropy, volume, pressure, coordination number and the distribution of interparticle forces to fully characterize the scaling laws near the jamming transition from a statistical mechanics point of view.

We also study the energy-landscape network. We find the stable basins and the first order saddles connecting them, and identify them with the network nodes and links, respectively. We analyze the network properties and model the system's evolution.

Acknowledgements

I am deeply grateful to my supervisor, Professor Hernán A. Makse, Physics Department and Levich Institute, City College of New York, for his important support and constructive comments throughout this work.

I am also grateful for the privilege of working closely with my colleagues Dr. Chaoming Song and Dr. Ping Wang, Physics Department, Physics Department and Levich Institute, City College of New York. Without their insightful projects this work would not be possible.

In addition, I wish to express my thanks to our group members Dr. Chris Briscoe, Dr. Diego Rybski, Dr. Hernán Rozenfeld, Dr. Lazraros Gallos, and Yuliang Jin, for useful discussions.

Lastly, I would like to thank my parents for their support throughout my academic career.

Contents

List of Figures

Chapter 1

Features of the Potential Energy Landscape

1.1 Introduction

An appealing approach for understanding out-of-equilibrium systems is to study the properties of the system's Potential Energy Landscape (PEL) [11] described by the $3N$-coordinates of all particles in the multi-dimensional configuration space, or landscape, of the potential energy of the system (N is the number of particles). Characterizing such potential energy landscapes has become an important approach to study the behavior of out-of-equilibrium systems. For example, this approach has provided important new insights into the origin of the unusual properties of supercooled liquids, such as the distinction between "strong" and "fragile" liquids [12].

The formalism introduced by Goldstein [13] consists of partitioning the poten-

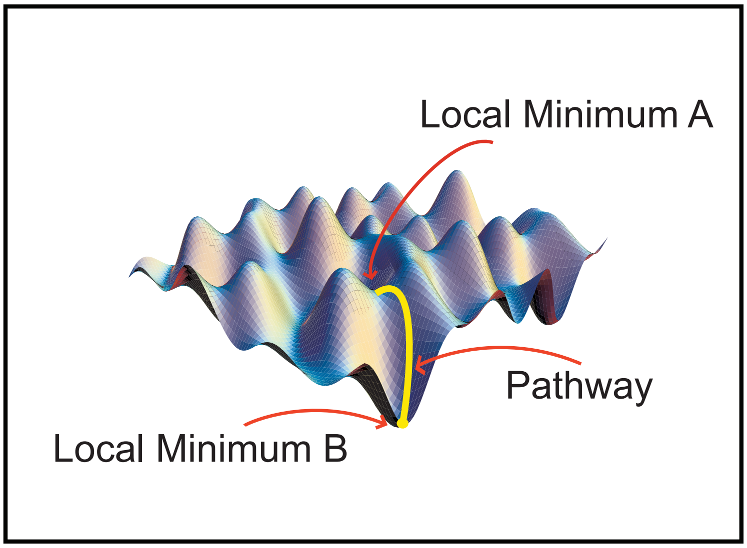

Figure 1.1: A model two-dimensional potential energy surface. The energy landscape is divided into basins of attraction, where the minima are represented by points and the pathway by the thick line.

tial energy surface into a set of basins as schematically illustrated in Fig. 1.1. The equilibrium dynamics on the potential energy surface can be separated into two types: the vibrational motion inside each basin and the transitional motion between the local minima. Stillinger and coworkers [14] developed the method of inherent structure to characterize the PEL. In this method, a local minimum in the PEL is located by following the steepest-descent pathway from any point surrounding the minimum. The inherent structure formalism simplifies the energy landscape into local minima and ignores the vibrational motion around them. The dynamics between the inherent structures is introduced with the transition states identified with the saddle points in the PEL. The transition states are stationary points like the local minima but they have at least one maximum eigendirection. The inherent structures are the jammed states in granular matter opening the possibility of a relation between jamming and the glass transition [15].

1.2 Finding Stationary Points

For the simplest system of N structureless particles possessing no internal orientational and vibrational degrees of freedom, the landscape is a $(3N+1)$-dimensional object. The potential energy function of this N-body system is $E(r_1, \ldots, r_N)$, where the vectors r_i comprise position coordinates. As mentioned above, the most interesting points of a potential energy surface are the stationary points, where the gradient vanishes. Here we explain how to locate these stationary points.

1.2.1 General Method – Newton-Raphson Method

Considering the Taylor expansion of a potential energy, E, around a general point in configuration space, X,

$$E(X+h) = E(X) + g^T h + \frac{1}{2} h^T H h + O(h^3), \tag{1.1}$$

where g is the gradient, H is the Hessian matrix as following: $g_i = \partial_i E$, $H_{ij} = \partial_i \partial_j E$, and h is a small step vector that gives the displacement away from X.

By Eq. 1.1, the calculation of energy difference for a given step h from initial point X is complicated. By selecting the eigenvectors of Hessian matrix e_α as our local coordinates, we can simplify the Taylor expansion of Eq. 1.1 as:

$$\triangle E = E(X+h) - E(X) \approx \sum_\alpha (g_\alpha h_\alpha + \frac{\lambda_\alpha}{2} h_\alpha^2), \tag{1.2}$$

where $g = \sum_\alpha g_\alpha e_\alpha$, $h = \sum_\alpha h_\alpha e_\alpha$, $He_\alpha = \lambda_\alpha e_\alpha$, and λ_α is the eigenvalue of Hessian matrix for component α.

From Eq. 1.2, it's easy to see under this local coordinates, the total change of energy could simply be the sum of the changes in each directions. This may help us to raise the energy in some directions and reduce the energy at others, and finally reach a stationary point. The length of each step components can be selected as the maximum change of energy:

$$h_\alpha = S_\alpha \frac{g_\alpha}{\lambda_\alpha}, \tag{1.3}$$

as shown in Fig.1.2. The sign $S_\alpha = \pm 1$ before the formula depends on the choice of uphill or downhill. Actually for $\lambda_\alpha > 0$, it's possible to choose another step for uphill case, since the $\triangle E_\alpha$ will increase as $|h_\alpha|$, but note for big step, the Taylor expansion (1.1) will not work any more, that require us to control the step length. And for $\lambda_\alpha < 0$, we obtain a opposite conclusion.

The stationary points, in this local coordinates representation, have the gradient $g_\alpha = 0$ for all α, and the eigenvalues of the Hessian matrix ordered according to

$$0 \leq \lambda_1 \leq \lambda_2 \cdots \leq \lambda_{3N} \tag{1.4}$$

for a minimum,

$$\lambda_1 \leq \lambda_2 \cdots \leq \lambda_{3N} \leq 0 \tag{1.5}$$

for a maximum, and

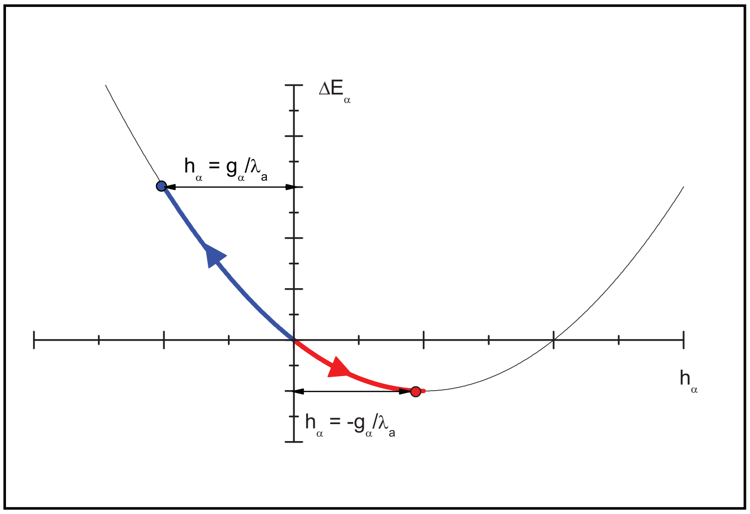

Figure 1.2: A schematic energy change curve for one component with $\lambda_\alpha > 0$. We can select the downhill step as $h_\alpha = -\frac{g_\alpha}{\lambda_\alpha}$ to obtain a maximum energy change. The uphill step can not be too big since the Taylor expansion will not be accurate enough for the calculation. Here, the uphill step is chosen as $h_\alpha = \frac{g_\alpha}{\lambda_\alpha}$

$$\lambda_1 \leq \cdots \leq \lambda_\alpha \leq 0 \leq \lambda_{\alpha+1} \leq \cdots \leq \lambda_{3N} \tag{1.6}$$

for a saddle point of order α.

The above general procedure, in the neighborhood of a minimum ($\lambda_\alpha \geq 0, \alpha = 1, \cdots, 3N$) takes a step in the direction opposite to the gradient along each e_α. That is, it steps toward the minimum. Similarly, it steps along the gradient toward the maximum. Generally, this algorithm steps toward the nearest stationary point on the surface by following opposite ($\lambda_\alpha \geq 0$) and along ($\lambda_\alpha \leq 0$) the various gradient directions.

1.2.2 Finding local minima – LBFGS

It is much easier to locate local minima than saddle points because, for the first, we only need to search downhill in every direction. At present one of the most efficient methods to search the local minima for large system is Nocedal's limited memory Broyden-Fletcher-Goldfarb-Shanno algorithm (LBFGS) [16, 17]. The LBFGS algorithm is a Greedy algorithm to solve nonlinear optimization problems. In the Newton-Raphson method discussed above, the Hessian matrix of second derivatives needs to be evaluated. Instead, the Hessian matrix used in the LBFGS method is approximated using updates specified by gradient evaluations from a previous point. Since it is only necessary to calculate the gradients at each searching step and not the Hessian, the LBFGS algorithm increases the computational speed of the algorithm enormously. The LBFGS algorithm can be obtained from http://www.netlib.org/opt/index.html. Here we present a brief explanation of the algorithm.

From an initial random point r_0 and an approximate Hessian matrix H_0 (in practice, H_0 can be initialized with $H_0 = I$), the following steps are repeated until r converges to the local minimum.

- Obtain a direction h_k by solving:

$$H_k h_k = -\nabla E(r_k).$$

- Perform a line search to find an acceptable step size γ_k in the direction found in the first step, then update $r_{k+1} = r_k + \gamma_k h_k$.

- Set, $s_k = \alpha_k h_k$.
- Set, $y_k = \nabla E(r_{k+1}) - \nabla E(r_k)$.
- Set the new Hessian:

$$H_{k+1} = H_k + \frac{y_k y_k^T}{y_k^T s_k} - \frac{H_k s_k (H_k s_k)^T}{s_k^T H_k s_k}.$$

1.2.3 Finding saddles – Eigenvector Following

A particular powerful method for locating saddle points is the eigenvector following method [11]. The eigenvector-following method, developed by Cerjan, Miller and others [11, 18, 19, 20, 21, 22], consists of locating a saddle point from a local minimum. At each searching step towards a saddle point with α order, the directions are separated into two types: α uphill directions to maximization and $3N - \alpha$ downhill directions to minimization.

We follow the implementation of the eigenvector-following method by Grigera [19]. In what follows, give a general description: at each searching step, a step size h is calculated by the diagonalized Hessian matrix [19, 21, 22]:

$$h_\alpha = S_\alpha \frac{2g_\alpha}{|\lambda_\alpha| \left(1 + \sqrt{1 + 4g_\alpha^2/\lambda_\alpha^2}\right)}, \tag{1.7}$$

where λ_α are the eigenvalues of the Hessian matrix and g_α are the components of the gradient in the diagonal base (h_α is set to 0 for the directions where $\lambda_\alpha = 0$). The sign $S_\alpha = \pm 1$ is chosen by the order of the saddle point. For a saddle point of order n, the algorithm will set $S_\alpha = -1$ for $1 \leq \alpha \leq n$ and $S_\alpha = 1$ for $\alpha > n$.

When $g_\alpha \to 0$, the step size h_α converges to the Newton-Raphson step as Eq. (1.3):

$$h_\alpha = S_\alpha \frac{g_\alpha}{\lambda_\alpha} + O(g_\alpha^2). \tag{1.8}$$

1.2.4 An Example

Here we generate a two dimensional soft-ball system in sphere boundary, which contains 31 particles with same radius. The interaction between particles (also for the interaction between particles and wall) follows as herzian law below:

$$V(r_i, r_j) = \epsilon |r1 - r2 - 2R|^{\frac{5}{2}} \tag{1.9}$$

Here, ϵ is the interaction strength between particles i and j, R is the radius of the particle. The volume fraction $\phi = 0.80$ (ϕ is the volume fraction of N particles of volume V_g), which is close to the glass transition of $2d$ hard sphere case. We first generate a random packing of the system, which is a initial point of the energy landscape. With the LBFGS method, we search the local minimum A nearby this initial point. After the minimum A obtained, we apply the eigenvector following method to walk from the point A on the potential energy surface to locate the transition state C (here the transition state is a first order saddle). Finally, the minimum B is located by applying LBFGS method again. Fig. 1.3 shows configurations of two local minima(marked as red) and the transition state (marked as blue) between them.

The pathway from minimum A to minimum B, passing by transition state C, is shown in Fig. 1.4. The pathway distance is the Euclidean distance,

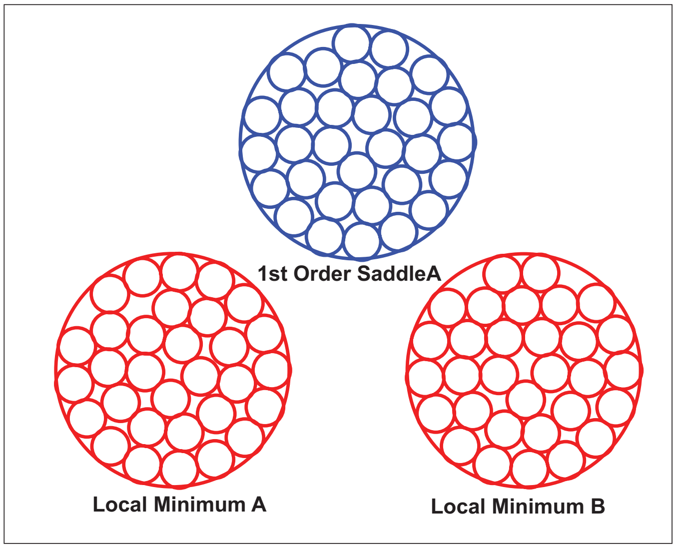

Figure 1.3: A two dimensional 31 particle system in sphere boundary. Three different configurations in this system are generated with different algorithms. The LBFGS method is applied to locate minima A and B. And for saddle C which connects A and B, the eigenvector following method is used.

$$d = \sqrt{(r'-r)\dot{(}r'-r)} = \sqrt{\sum_{i,\alpha}(r'_{i,\alpha} - r_{i,\alpha})^2}, \tag{1.10}$$

where $i = 1, 2, 3$, $\alpha = 1 \cdots 3N$, r' is the coordinate of configuration passing along the searching method and r is the coordiante of saddle C.

1.3 Describing the Potential Energy Landscape

The dynamics from minimum to minimum can be represented as a walk on a network whose nodes correspond to the minima and where edges link those minimum which are directly connected by a transition state. Fig. 1.5 [23] provides an illustration of such an landscape network for a two-dimensional energy surface.

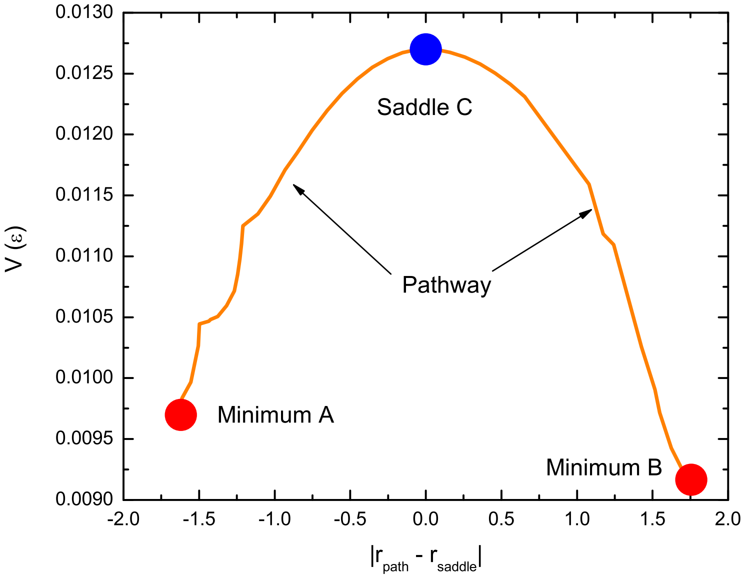

Figure 1.4: The pathway from minimum A to minimum B, passing by the saddle C, the x-coordinate is the distance from saddle C, the y-coordinate is the potential energy of the packing.

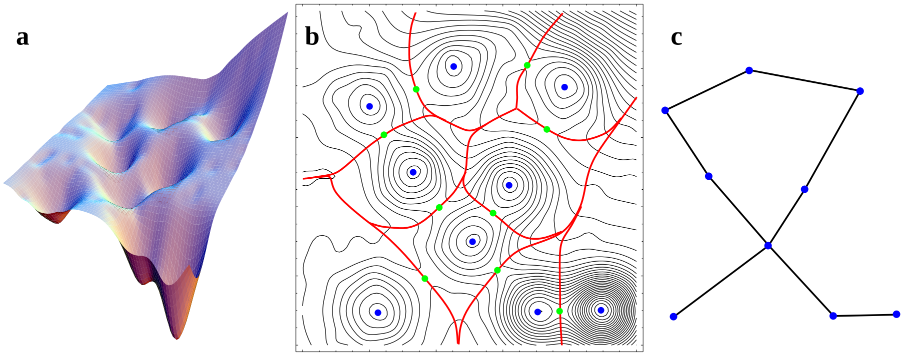

Figure 1.5: (a) A model two-dimensional potential energy surface. (b) The contour plot of this surface showing the inherent structure division of the energy landscape into basins of attraction (the minima and transition states are represented by points and the basin boundaries by the thick lines). (c) The representation of the landscape as a network (from [23]).

To characterize the topology of the landscape network, J.Doye[23] study small Lennard-Jones clusters to locate nearly all the minima and transition states on the potential energy landscape. The inherent structure network of such a system has a scale free and small world properties. Here the basic energy landscape network properties are given as below.

1.3.1 Scale Free

The study of real complex networks has revealed that many of them share some fundamental common properties. Of great importance is the form of the degree distribution for these networks, which is unexpectedly wide. This means that the degree of a node may assume values that span many decades. Thus, although the majority of nodes have a relatively small degree, there is a finite probability that a few nodes will have degree of the order of thousands or even millions. Networks that exhibit such a wide distribution $P(k)$ are known as scale-free networks, where the term refers to the absence of a characteristic scale in the degree k. This distribution very often obeys a power-law form with a degree exponent γ, usually in the range $2 < \gamma < 4$ [24],

$$P(k) \sim k^{-\gamma} \,. \tag{1.11}$$

Scale-free networks are noteworthy because many empirically observed networks appear to be scale-free, including the world wide web, the Internet, citation networks, and some social networks.

1.3.2 Small World

A more generic property, that is usually inherent in scale-free networks but applies equally well to other types of networks, such as in Erdős-Rényi random graphs, is the small-world feature. Originally discovered in sociological studies [25], it is the generalization of the famous 'six degrees of separation' and refers to the very small network diameter. Indeed, in small-world networks a very small number of steps is required to reach a given node starting from any other node. Mathematically this is expressed by the slow (logarithmic) increase of the average diameter of the network, $\bar{\ell}$, with the total number of nodes N, $\bar{\ell} \sim \ln N$, where ℓ is the shortest distance between two nodes and defines the distance metric in complex networks [24, 26, 27, 28], namely,

$$N \sim e^{\bar{\ell}/\ell_0}, \tag{1.12}$$

where ℓ_0 is a characteristic length.

Small world properties are found in many real world phenomena, including road maps, food chains, electric power grids, metabolite processing networks, networks of brain neurons, voter networks, telephone call graphs, and social influence networks.

1.3.3 An Example

Here we generate a small Lennard-Jones system without boundary condition. The Lennard-Jones potential between particles is:

$$V(r_i, r_j) = 4\epsilon \left[\left(\frac{\sigma}{r}\right)^{12} - \left(\frac{\sigma}{r}\right)^{6} \right], \tag{1.13}$$

where ϵ is the interaction strength between particles i and j, $r = |r_i - r_j|$ and σ is the characteristic size of the molecules. We construct the network of this small Lennard-Jones system by locating nearly all the minima and transition states on the potential energy landscape.

We repeated the main results as Doye studied, the numbers of minima and transition states are expected to increase roughly as $N_{min} \sim e^{\alpha N}$ and $N_{st} \sim Ne^{\alpha N}$ respectively, where N is the number of atoms in the cluster. Therefore, the largest network that we are able to consider is for a 14-atom cluster for which we have located 4158 minima and 90 738 transition states.

We examine the distributions for the numbers of connections for each node. We find that as the size of the cluster increases a clear power-law tail develops, which has a universal form independent of the cluster size (Fig. 1.6). The exponent of the power law, 2.78, is similar to other scale free networks[29]. The network is extremely heterogeneous with a few hubs that have a very large number of connections, but with the majority of nodes only connected to a relatively small number of other minima.

The average diameter between nodes of a small-world network scales logarithmically with network size, while the network is highly clustered. From Fig. 1.7, it is clear that the networks for the clusters show such feature and are small worlds.

The topology of the landscape network will of course significantly affect the dynamics. This connection can be probed for very small systems where the network can be completely characterized and the inherent structure dynamics obtained by a master equation approach. However, this approach is not practical for the system sizes that are of most interest. Therefore, models of the glass transition

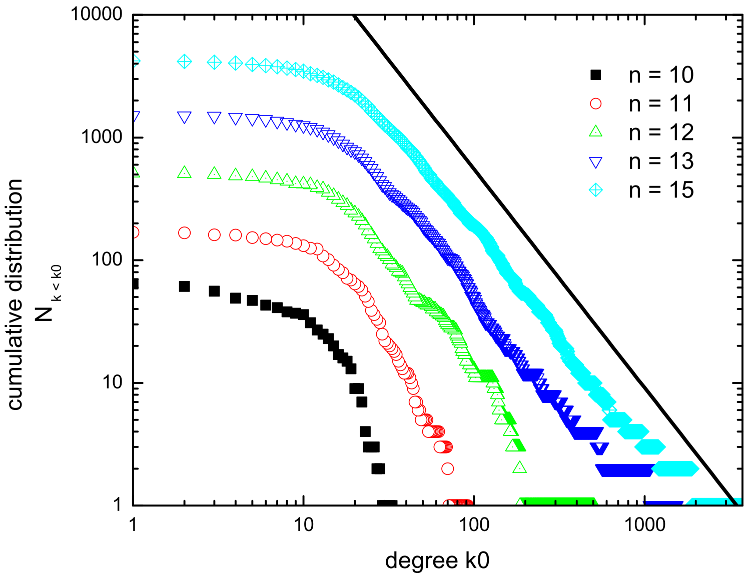

Figure 1.6: The cumulative distribution for the number of nodes that have more than k connections. The curves correspond to clusters of different sizes from $n = 10$ to $n = 14$. An additional straight line with slope $-(\gamma - 1)$, where $\gamma = 2.78$, has been plotted to emphasize the power law tail.

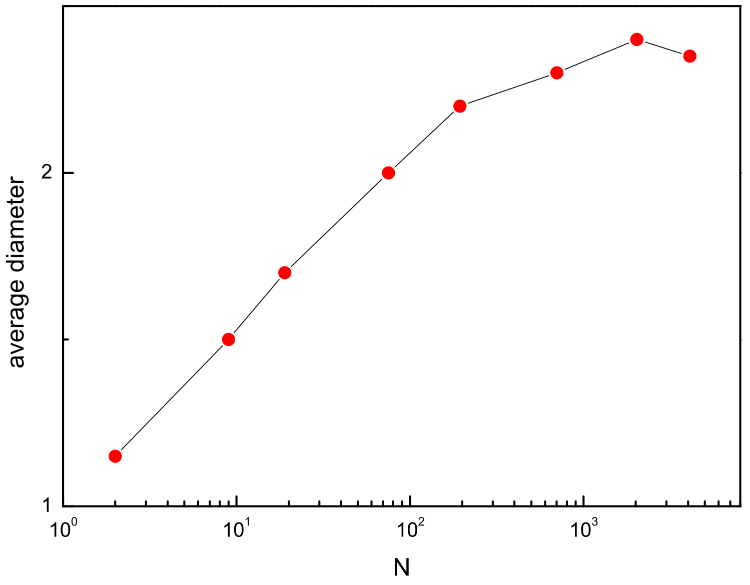

Figure 1.7: The dependence of the average diameter between nodes (in steps) on the size of the network, N. The data points are for Lennard-Jones clusters with from 7 to 14 atoms

usually have to assume a simplified topology for the interstate dynamics, or relate the dynamics to static quantities through phenomenological equations, such as the Adam-Gibbs equation which relates the relaxation time in supercooled liquids to the configurational entropy. To fully unlock the potential insights from the inherent structure view of the dynamics, a means of statistically modelling the network topology from a partial characterization of the potential energy landscape is therefore needed. Here in the next chapter, we present a statistical mechanical method to describe such complex system – jammed matter.

Chapter 2

Statistical Mechanics for Jammed Matter

The jammed state is defined as the condition when a many-body system is blocked in a configuration far from equilibrium, such that relaxation cannot occur within a measurable time-scale. Jamming has emerged as a governing feature in many systems, such as granular materials, emulsions, colloidal suspensions, structural glasses and spin glasses, among numerous others.

The above disordered systems are examples of non-equilibrium systems, wherein a state may occur having particles in close contact with one another and therefore experience a jamming transition. All these systems belong to a class of materials known as “soft” matter, referring to their complex mechanical properties, being neither fluid nor solid-like. The process of jamming is specific to each system based on their particular microscopic properties. For example, pouring a granular material into a closed container, accompanied by oscillation, is sufficient to achieve the jamming condition, while glasses can be cooled down to very low temperatures at which the molecules can no longer diffuse, thus resulting in a jammed configuration. Hence, through very different jamming mechanisms, the jammed state is achieved for a variety of systems.

2.1 Jamming in Particulate Systems

In a fluid at thermal equilibrium the particle dynamics is too fast to capture the detail of the underlying potential energy landscape, thus it appears flat. Decreasing the temperature slows down the Brownian dynamics, implying a limiting temperature below which the system can no longer be equilibrated in this way. Hence, the thermal system falls out of equilibrium on the time scale of the experiment and thus undergoes a glass transition [12]. The motion of each particle is no longer thermally activated and only the vibration inside the cage formed by its surrounding neighbours persists. However, even below the glass transition temperature the particles continue to relax, but the nature of the relaxation is very different to that in equilibrium. This phenomenon of a structural evolution beyond the glassy state is known as “aging”. The dynamics becomes dominated by the multidimensional potential energy surface which the system can explore as a function of the degrees of freedom of the particles, depicted in Fig. 2.1 [30]. In order to describe this landscape Stillinger and coworkers [14, 31], based on ideas introduced by Goldstein [13], developed the concept of inherent structures which are defined as the potential energy minima. The trajectory of a system aging at temperature T can be mapped onto the successive potential basins that the system explores.

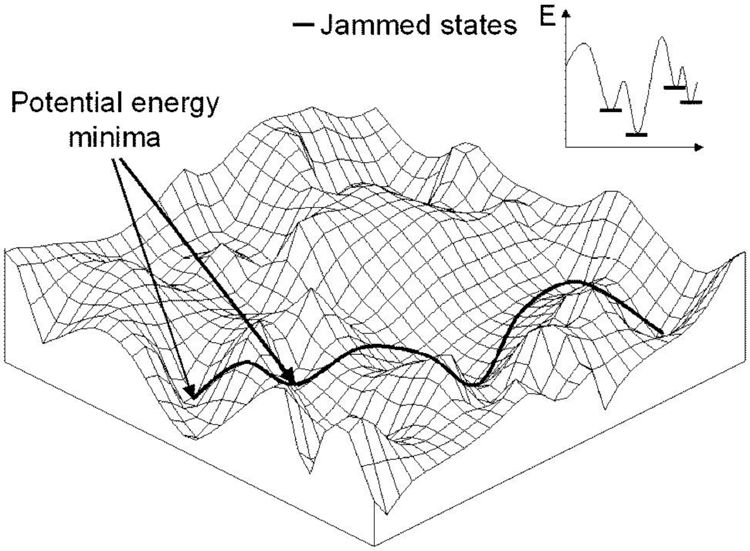

Figure 2.1: The multidimensional energy landscape dominates the dynamics below the glass transition, as the system explores the inherent structures defined as the potential energy minima. A trajectory through the landscape is shown and the analogy between these inherent structures and the jammed states in granular materials is examined (from [30]).

Computational methods are the only available technique for investigating this behaviour, in which the inherent structures are found via steepest-descent quenching of the system configurations to the basins of the wells. The entropy of the system can be shown to be separable into contributions from the available configurations and the vibrational modes around each minimum. There have been many studies which have embarked on an investigation of aging through the exploration of the configurational space [32, 33, 34].

The importance of the inherent structure formalism is in enabling the comparison of jamming in particulate systems with glasses [35]. The entropy arising from the inherent configurations of the glass at very low temperatures and the exploration of these configurations due to the vibrational modes of the particles could be viewed as analogous to the configurational changes in particulate packings under slow tapping or shear. However, in granular materials there is an added effect of friction, which dissipates the analogous vibrations at once. Unlike granular materials, a thermal system is never permanently trapped in the bottom of a valley, but escapes in other accessible unstable directions through intrinsic thermal vibrations. At any finite temperature the system will not resemble the granular system in that it continuously evolves toward a maximum density state. Thus, the only true analogous situation between glasses and granular materials is valid at zero temperature. However, there are characteristic features of the glassy relaxation at a finite T which act as useful tools for the description of granular systems by exploiting the analogy between the relaxation of powders and aging in glassy systems [36].

For instance, theories developed during the late eighties and nineties in the field of spin glasses [37, 38, 39] have led to a better understanding of glassy systems through the generalisation of usual equilibrium relations, such as the fluctuation-dissipation relation, to situations far from equilibrium [40]. This approach developed by Cugliandolo, Kurchan and collaborators yielded macroscopic observable properties, such as an "effective temperature" for the slow modes of relaxation, which could then be compared between various glassy systems. Furthermore, the existence of an effective temperature with a thermodynamic meaning in glasses at very low temperature suggests an 'ergodicity' for the long-time behaviour of the system [41]. This ergodicity is closely related to the statistical ideas for granular systems [42, 43, 44] which we will introduce in the following sections. In support of this argument, the effective temperature in glasses is found to be an adequate concept for describing granular matter [45].

In a sense one would imagine there is no simpler physical system than a granular assembly. After all it is just a set of packed rigid objects with no interaction energy. It is the inability to describe the system on the continuum level in any other way except according to its geometry which has led to a lack of a well established granular theory until present. Mostly due to their industrial importance, there has been a vast literature describing phenomenological observations without an encompassing theory. In the words of de Gennes, the state of granular matter can be compared to solid state physics in the 30's or critical phenomena in phase transitions before the renormalization group. In other words, there is a need for describing the universal features of the observed behaviour within a theoretical framework devised for these and other jammed systems.

In parallel with the extensive research on glasses, described earlier, a decade ago Edwards and collaborators postulated the existence of a statistical ensemble for granular matter, despite the lack of thermal motion and the absence of an equilibrium state [3, 46, 47, 48, 49]. The main postulate was based on jamming the granular particles at a fixed total volume such that all microscopic jammed states are equally probable and become accessible to one another (ergodic hypothesis) by the application of a type of external perturbation such as tapping or shear, just as thermal systems explore their energy landscape through Brownian motion. Hence, let us consider granular jamming in more detail.

In terms of physics, in particulate materials such as emulsions and granular media, a jammed system results if particles are packed together so that all particles are touching their neighbours, which obviously requires a sufficiently high density. In these athermal systems there is no kinetic energy of consequence; the typical energy required to change the positions of the jammed particles is very large compared to the thermal energy at room temperature ($\sim 10^{14}$ times). As a result, the material remains arrested in a static state and is able to withstand a sufficiently small applied stress.

It turns out that by allowing the system to explore its available configurational space through external mechanical perturbations, the system will rearrange such that all possible configurations become accessible to one another. Continuing with the analogy in the real world, the gentle tapping on a table of the cup filled with sugar will initially change the unstable angle of repose of the sugar pile and flatten its top surface, and therefore its density, until it settles into a desired configuration which depends on the strength of the tap. We can only perform a statistical analysis on the resulting configurations which have no memory of their creation, i.e. the true jammed configurations. Thus we arrive at a jammed ensemble, suitable for the application of statistical mechanics. Since the particles can jump across the energy landscape during the tap, but then stop at once due to frictional dissipation, there is an analogy to the inherent structure formalism in glassy systems [43]. This new statistical mechanics is able to provide unifying concepts between previously unrelated media.

2.2 Achieving the jammed state

Experimentally, the conditions for a statistical ensemble of jammed states can be achieved by pre-treating the granular assembly by tapping or via slow shear-

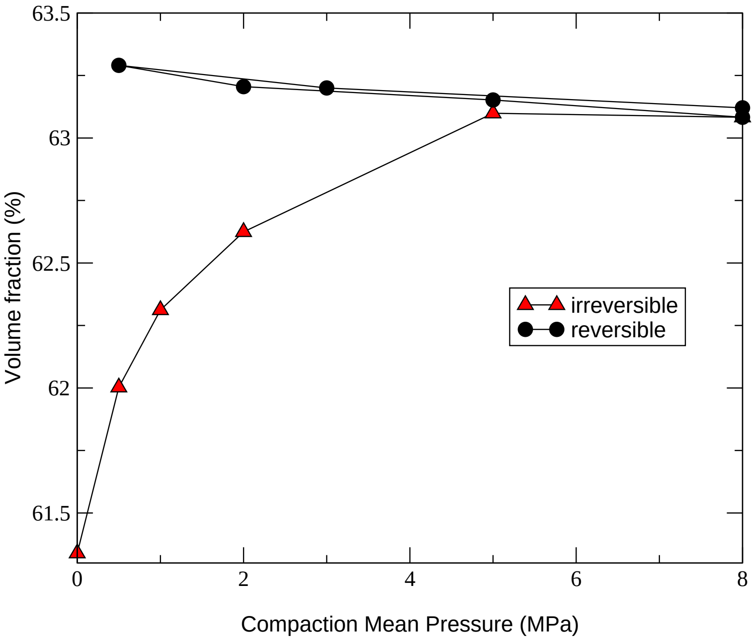

Figure 2.2: Compaction curve for a packing of glass beads under an oscillating pressure. Increasing the amplitude of oscillation initially increases the density by filling the loose voids, after which a reversible regime is achieved (from [53]).

driving. Experiments at the University of Chicago involving the tapping of granular columns were the first to show the existence of a reversible regime in which the system configurations are independently sampled [50]. Starting with a loose packing of the grains, the tapping routine initially removes the unstable loose voids and thus eliminates the irreversible grain motion. Once all the grains are touching their neighbours, the density of the resulting configuration becomes dependent on the tapping amplitude and the number of taps; the larger the amplitude, the lower the density. The mechanism of the compaction process leading to a steady-state density is extremely slow, in fact, it is logarithmic in the number of taps. This dependence of the density of grains on the external perturbation of the system once the memory effects of the pile construction details have been removed, is known as the reversible branch of the 'compaction curve', see Fig. 2.2. Despite the presence of friction between grains (implying memory effects) this curve is reversible, establishing a new type of equilibrium states. It is along this curve that the thermodynamics for granular matter can be applied.

There have been several further experiments confirming these results for different system geometries, particle elasticities and compaction techniques. For example, the system can be mechanically tapped or oscillated, vibrated using a loudspeaker, slowly sheared in a couette geometry, or even allowed to relax under large pressures over long periods of time, all to the same effect [51, 52, 53]. A new compaction regime is shown under an oscillating pressure where the same density dependence of a packing of glass and acrylic beads is noted for varying amplitudes of the pressure oscillation. These experiments have been performed at Schlumberger-Doll Research [53]. The resulting curve of the achieved volume fraction as a function of the amplitude of the pressure oscillation is shown in the inset of Fig. 2.2.

At this point, it is important to note that here only infinitely rigid, rough grains are considered in which an increase in the pressure of the system, for instance by placing a piston on top of the grains, causes no change in the shape of the grains and therefore no change in the packing density. On the other hand, real grains have a finite elastic modulus, thus the application of a sufficiently large external pressure will always result in grain deformation and therefore a density increase unrelated to the tapping. In soft particles, such as emulsions, the effect of pressure is more significant. The tapping experiment described above measured the resulting densities at atmospheric pressure, which is considered to be the zero reference pressure. The same experiment can be repeated at finite pressures giving rise to equivalent compaction curves, depicted in Fig. 2.3. Whereas hard grains, such as glass beads, require extremely large pressures ($\sim$ 1MPa) to deform and the amount of deformation is limited by their yield stress, softer particles, such as rubber, are able to reach higher densities with relative ease. Droplets and bubbles, being the softest particles one can have, are capable of reaching the density of 1, corresponding to a biliquid foam and a foam, respectively, by an application of much smaller pressures ($\sim$ 1kPa). They have the advantage of the whole pressure range being accessible to them. Another distinction between granular materials and emulsions is the presence of friction in the former and the smoothness of the latter. Since friction plays an important role in inducing memory into the system, its absence leads to a much easier achievement of the jammed state, described above. For instance, in the case of emulsions, allowing the particles to cream

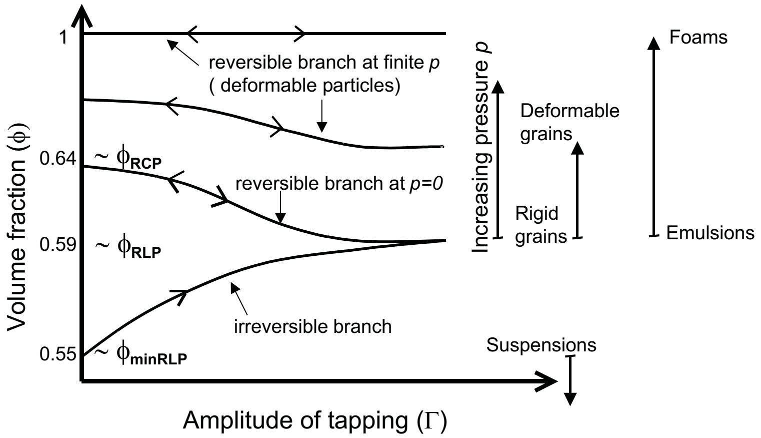

Figure 2.3: Compaction curves of volume fraction ϕ versus amplitude of oscillation A for different external confining pressures, p. Increasing the amplitude of oscillation initially increases the volume fraction by filling the loose voids (irreversible branch), after which a reversible regime is achieved. For infinitely rigid grains (the "zero pressure" curve) the minimum volume fraction along the irrevesible branch is the random loose packing. The reversible branch goes from the maximum random loose packing fraction to the random close packing fraction. Below the minimum RLP only suspensions can exist.

under gravity will suffice to arrive at the reversible part of the compaction curve, bypassing the irreversible branch.

2.3 Statistical Mechanics for Jammed Matter

This section aims to justify the use of statistical mechanics tools in situations where the system is far from thermal equilibrium, but jammed. In what follows, we present the classical statistical mechanics theorems to an extent which facilitates an understanding of the important concepts for the development of an analogous granular theory, as well as the assumptions necessary for the belief in such a parallel approach. Thereafter, we present a theoretical framework to fully describe the exact specificities of the granular packing, and the shaking scenario which leads to the derivation of the Boltzmann equation for a jammed granular system.

This kind of an analysis paves the path to macroscopic quantities, such as the compactivity, characterising each static configuration from the microstructural information of the packing. It is according to this theory that the jammed configurations obtained from experiments and simulations are later characterised.

2.3.1 Classical Statistical Mechanics

In the conventional statistical mechanics of thermal systems, the different possible configurations, or microstates, of the system are given by points in the phase space of all positions and momenta $\{p, q\}$ of the constituent particles. The equilibrium probability density ρ_{eqm} must be a stationary state of Liouville's equation which implies that ρ_{eqm} must be expressed only in terms of the total energy of the system, E [54]. The simplest form for a system with Hamiltonian $\mathcal{H}(p, q)$ is the microcanonical distribution:

$$\rho_{\text{eqm}}(E) = \frac{1}{\Sigma_{\text{eqm}}(E)}, \tag{2.1}$$

for the microstates within the ensemble, $\mathcal{H}(p, q) = E$, and zero otherwise. Here,

$$\Sigma_{\text{eqm}}(E) = \int \delta(E - \mathcal{H}(p, q)) \;\; dp \; dq, \tag{2.2}$$

is the area of energy surface $\mathcal{H}(p, q) = E$.

Equation (2.1) states that all microstates are equally probable. Assuming that this is the true distribution of the system implies accepting the ergodic hypothesis, i.e. the trajectory of the closed system will pass arbitrarily close to any point in phase space.

It was the remarkable step of Boltzmann to associate this statistical concept of the number of microstates with the thermodynamic notion of entropy through his famous formula

$$S_{\mathrm{eqm}}(E) = k_B \log \Omega_{\mathrm{eqm}}(E). \tag{2.3}$$

Thus, in classical statistical mechanics, the total energy of the system is sufficient to describe the probability density of states. Whereas the study of thermal systems has had the advantage of available statistical mechanics tools for the exploration of the phase space, an entirely new statistical method, unrelated to the temperature, had to be constructed for grains.

2.3.2 Statistical Mechanics for Jammed Matter

A large body of experiments, theory and simulations have focused on the study of volume fluctuations in granular media [2, 35]. Statistical studies have been concerned with testing for the existence of thermodynamics quantities such as effective temperatures and compactivity as well as challenging the foundations based on the ergodic hypothesis or equal probability of the jammed states.

Unfortunately, there is no first principle derivation of the granular statistical mechanics analogous to the Liouville theorem for equilibrium systems [54]. Therefore, advancing the statistical mechanics of granular matter requires well-defined theoretical predictions that can be tested experimentally or numerically. While the possibility of a thermodynamic principle describing jammed matter is recognized as a sensible line of research, the problem with the statistical approach is that after almost 20 years there are no practical applications yet, such as predictions of equations of state relating the observables: pressure, volume, coordination number, entropy, etc, that may lead to new phenomena to be discovered and tested experimentally that will allow for a concrete exploitation of the thermodynamic framework.

Here, a systematic study of the volume-stress ensemble of jammed matter is developed. Systems of interest are primarily packings of granular materials, frictional colloids, infinitely rough grains and frictionless droplets mimicking concentrated emulsions.

Sphere packing problem

Filling containers with balls is one of the oldest mathematical puzzles known to scientists. The study of this problem started four centuries ago when Johannes Kepler conjectured that the most efficient arrangement of spheres is the FCC lattice (an important part of the 18th problem proposed by Hilbert in 1900). Even though this is a tool used for centuries in fruit markets around the globe, nearly 400 years passed before this conjecture was considered a mathematical proof, which has been developed only recently by Hales [55] in a series of articles covering 250 pages supplemented by 3Gb of computer code to determine the best ordered packing through linear programming. The difficulty arises since in 3d it is not enough to look at the packing of one cell, but it is necessary to consider several Voronoi cells at once. That is, the packing that minimize the volume locally (the dodecahedron) does not tile the system globally. Such a situation does not arise in 2d, where the hexagonal packing minimizes the volume locally and globally; the Kepler conjecture in 2d was proved long ago.

The analogous problem for disordered packings has also an illustrious but unfinished history. This problem was initiated by the pioneering work of Bernal in the 1960's [56] (although earlier attempts can be found). The traditional view states that [57] "packings of spherical particles have been shaken, settled in different fluids and kneaded inside rubber balloons and all with no better results than a maximum density of 63%". This is the so-called random close packing RCP limit [56, 57, 58, 59]. On the other hand, other experiments have shown that densities as low as 55% can be obtained in random loose packings, RLP [58, 59, 60]. To this date there is no physical explanation of this phenomenon, no theoretical prediction of such density values and heated debates are still found in the literature regarding the existence of rigorous definitions of the RCP and RLP, the uniqueness of the RCP state and the nature of their state of randomness.

Statistical mechanics of jammed matter

Conventional Statistical Mechanics uses the ergodic hypothesis to derive the microcanonical and canonical ensembles, based on the quantities conserved, typically the energy E [54]. The analogous development of a statistical mechanics of granular and other jammed materials presents many difficulties. First, the macroscopic size of the constitutive particles forbids the equilibrium thermalization of the system. Second, the fact that energy is constantly dissipated via frictional interparticle forces further renders the problem outside the realm of equilibrium statistical mechanics due to the lack of energy conservation. In the absence of energy conservation laws, a new ensemble is needed in order to describe the system properties.

Following this theoretical perspective, Edwards proposed the statistical mechanics of jammed matter and interest in the problem of volume fluctuations has flourished [47]. The central concept is that of a volume function $\mathcal{W}$ replacing the role of the Hamiltonian in describing the microstates of the system in the volume-ensemble and the stress boundary $\Pi = \int \sigma_{ij} dV$ with the stress $\sigma_{ij} = 1/(2V) \sum_c f_i^c r_j^c$ describing the stress-ensemble [7, 10], where f_i^c, r_i^c are the force and position at contact c. For simplicity only the isotropic case is described. Thus, only the pressure $\sigma = (\sigma_{ii} + \sigma_{jj} + \sigma_{kk})/3$ is necessary to describe force fluctuations.

If the space associating each particle is partitioned by its surrounding volume, $\mathcal{W}_i$ (for instance with a Voronoi tessellation as it will be done bellow), then the total volume, $\mathcal{W}$, of a system of N particles is given by:

$$\mathcal{W} = \sum_{i=1}^{N} \mathcal{W}_i. \tag{2.4}$$

The ensemble average of the volume function $\mathcal{W}$ provides the volume of the system, $V = \langle \mathcal{W} \rangle$, in an analogous way to the average of the Hamiltonian is the energy in the canonical ensemble of equilibrium statistical mechanics.

Angoricity and Compactivity

The full canonical partition function in the volume-stress ensemble is the starting point of the statistical analysis [7]:

$$\mathcal{Q}(X,A) = \int g(\mathcal{W},\Pi)\ \exp\Big[-\frac{\Pi}{A}-\frac{\mathcal{W}}{X}\Big]\ \Theta_{\rm jam}\ d\mathcal{W}\ d\Pi, \tag{2.5}$$

where $g(\mathcal{W},\Pi)$ is the density of states for a given volume and boundary stress. Here $\Theta_{\rm jam}$ formally imposes the jamming restriction and therefore defines the ensemble of jammed matter. This crucial function will be discussed at length below. As a minimum requirement it should ensure touching grains, and obedience to Newton's force laws.

Just as $\partial E/\partial S = T$ is the temperature in equilibrium systems, the temperature-like variables in granular systems are the compactivity [47]:

$$X = \frac{\partial V}{\partial S}, \tag{2.6}$$

and the angoricity [from the Greek "$\acute{\alpha}\gamma\chi o\zeta$" (ankhos) = stress] [7]:

$$A = \frac{\partial \Pi}{\partial S}. \tag{2.7}$$

Here, we test the idea of this combined volume-stress ensemble in the next chapter.

Chapter 3

The Jamming Transition in Soft Particulate Matter

3.1 Introduction

The application of concepts from equilibrium statistical mechanics to out of equilibrium systems has a long history of describing diverse systems ranging from glasses to granular materials [1, 2, 47]. For dissipative jammed systems– particulate grains or droplets– a key concept is to replace the energy ensemble describing conservative systems by the volume ensemble [47]. However, this approach is not able to describe the jamming critical point (J-point) for deformable particles like emulsions [4, 5, 6], whose geometric configurations are influenced by the applied external stress. Therefore, the volume ensemble requires augmentation by the ensemble of stresses [7, 8, 9, 10]. Just as volume fluctuations can be described by compactivity, the stress fluctuations give rise to an angoricity, another analogue of temperature in equilibrium systems. Here, we test the combined volume-stress ensemble by comparing the statistical properties of jammed configurations obtained by dynamics with those averaged over the ensemble as a probe ergodicity. Agreement between both methods supports the idea of "thermalization" at a given angoricity and compactivity. These intensive variables elucidate the thermodynamic order of the jamming phase transition by showing the absence of critical fluctuations above jamming in static observables like pressure and volume. Our results promote the possibility of calculating important quantities such as the distribution of forces, entropy and ensemble average of volume, pressure and coordination number to fully characterize the scaling laws near the jamming transition using a statistical mechanics ensemble.

3.2 Angoricity and Compactivity of Jamming

A granular system compresses into a mechanically stable configuration at a nonzero pressure in response to the application of an external strain [1, 2, 4]. This process is typically referred to as the jamming transition and occurs at a critical volume fraction ϕ_c [4]. The application of a subsequent external pressure with the concomitant particle rearrangements and compression results in a set of configurations characterized by the system volume $V = NV_g/\phi$ (ϕ is the volume fraction of N particles of volume V_g) and applied external stress or pressure p (for simplicity we assume isotropic states). It has been long argued whether the jamming transition is a first-order transition at the discontinuity in the average coordination number, $\langle Z\rangle$, or a second-order transition with the power-law scaling of the system's pressure as the system approaches jamming with $\phi - \phi_c \to 0^+$ [5, 6, 61, 62]. Previous work [10, 63, 64] has proposed to explain the jamming transition by a field theory in the pressure ensemble. Here, we use the idea of "thermalization" of an ensemble of mechanically stable granular materials at a given volume and pressure to study the jamming transition from a thermodynamic viewpoint.

For a fixed number of grains, there exist many jammed states [65] confined by the external pressure p in a volume V. In an effort to describe the nature of this nonequilibrium system from a statistical mechanics perspective, a statistical ensemble [7, 9, 10] was introduced for jammed matter. In the canonical ensemble of pressure and volume, the probability of a state is given by $\exp[-\mathcal{W}(\partial S/\partial V) - \Gamma(\partial S/\partial \Gamma)]$, where S is the entropy of the system, $\mathcal{W}$ is the volume function measuring the volume of the system as a function of the particle coordinates and $\Gamma \equiv pV$ is the boundary stress (or internal virial) [63] of the system. Just as $\partial E/\partial S = T$ is the temperature in equilibrium system, the temperature-like variables in jammed systems are the compactivity $X = \partial V/\partial S$ [47] and the angoricity $A = \partial \Gamma/\partial S$ [7].

In a recent paper [66] the compactivity was used to describe frictional hard spheres in the volume ensemble. Here, we test the validity of the statistical approach in the combined pressure-volume ensemble to describe deformable, frictionless particles, such as emulsion systems jammed under osmotic pressure near the jamming transition [67]. We demonstrate that the jamming transition can be probed thermodynamically by a "jamming temperature" T_{J} comprised of contributions from the angoricity A and the compactivity X. The calculation of jamming "heat" capacities characterizes the system fluctuations and shows the lack of critical fluctuations in the static quantities as the jamming transition point is approached from above $\phi \to \phi_c^+$. Thus, the thermodynamical viewpoint determines the order of the phase transition and allows one to calculate the physical observables near jamming.

In general, if the density of states $g(\Gamma, \phi)$ in the space of jammed configurations (defined as the probability of finding a jammed state at a given (Γ, ϕ) at $A = \infty$) is known, then calculations of macroscopic observables, like pressure p and average coordination number Z as a function of ϕ, can be performed by the canonical ensemble average [63, 64] at a given volume:

$$\langle p(\alpha, \phi) \rangle_{\text{ens}} = \frac{1}{\mathcal{Z}} \int_0^\infty p \; g(\Gamma, \phi) \; e^{-\alpha\Gamma} \; \mathrm{d}\Gamma, \tag{3.1}$$

and

$$\langle Z(\alpha, \phi) \rangle_{\text{ens}} = \frac{1}{\mathcal{Z}} \int_0^\infty Z \; g(\Gamma, \phi) \; e^{-\alpha\Gamma} \; \mathrm{d}\Gamma, \tag{3.2}$$

where the canonical partition function is $\mathcal{Z} = \int_0^\infty g(\Gamma, \phi) e^{-\alpha\Gamma} \mathrm{d}\Gamma$ and the density of states is normalized as $\int_0^\infty g(\Gamma, \phi) \mathrm{d}\Gamma = 1$. The inverse angoricity is defined as $\alpha \equiv 1/A = \partial S / \partial \Gamma$.

At the jamming transition the system reaches isostatic equilibrium, such that the stresses are exactly balanced in the resulting configuration, and there exists a unique solution to the interparticle force equations satisfying mechanical equilibrium. It is well known that observables present power-law scaling [5, 6]:

$$\langle p \rangle_{\text{dyn}} \sim (\phi - \phi_c)^a \,, \qquad \langle Z \rangle_{\text{dyn}} - Z_c \sim (\phi - \phi_c)^b, \tag{3.3}$$

where $a = 3/2$ and $b = 1/2$ for Hertzian spheres and $Z_c = 6$ is the coordination number at the isostatic point (J-point) [5]. The average $\langle \cdots \rangle_{\text{dyn}}$ indicates that these quantities are obtained by averaging over packings generated dynamically in either simulations or experimentally as opposed to the ensemble average over configurations $\langle \cdots \rangle_{\rm ens}$ of Eqs. (3.1)–(3.2). Comparing the ensemble calculations, Eq. (3.1)–(3.2), with the direct dynamical measurements, Eq. (3.3), provides a basic test of the ergodic hypothesis for the statistical ensemble.

Our approach is the following: We first perform an exhaustive enumeration of configurations to calculate $g(\Gamma, \phi)$ and obtain $\langle p(\alpha, \phi) \rangle_{\rm ens}$ as a function of α for a given ϕ using Eq. (3.1). Then, we obtain the angoricity by comparing the pressure in the ensemble average with the one obtained following the dynamical evolution with Molecular Dynamics (MD) simulations. By setting $\langle p(\alpha, \phi) \rangle_{\rm ens} = \langle p \rangle_{\rm dyn}$, we obtain the angoricity as a function of ϕ. By virtue of obtaining $\alpha(\phi)$, all the other observables can be calculated in the ensemble formulation. The ultimate test of ergodicity is realized by comparing the remaining ensemble observables with the corresponding direct dynamical measures.

3.2.1 Ensemble Calculations

The density of jammed states $g(\Gamma, \phi)$ is calculated in the framework of the potential energy landscape (PEL) formulation introduced by Goldstein [13] and Stillinger-Weber [31, 32] to describe supercooled liquids. In the case of frictionless jammed systems, the mechanically stable configurations are defined as the local minima of the potential energy surface (PES) of the system [5, 65] (see Fig. 3.1 inset for a schematic representation). In the simulations, two spherical soft particles in contact interact via a normal Hertz force [61, 68], $F_n \propto (\delta r)^{\delta}$, where δr is the normal overlap between the spheres under deformation and $\delta = 1.5$, in a periodically re-

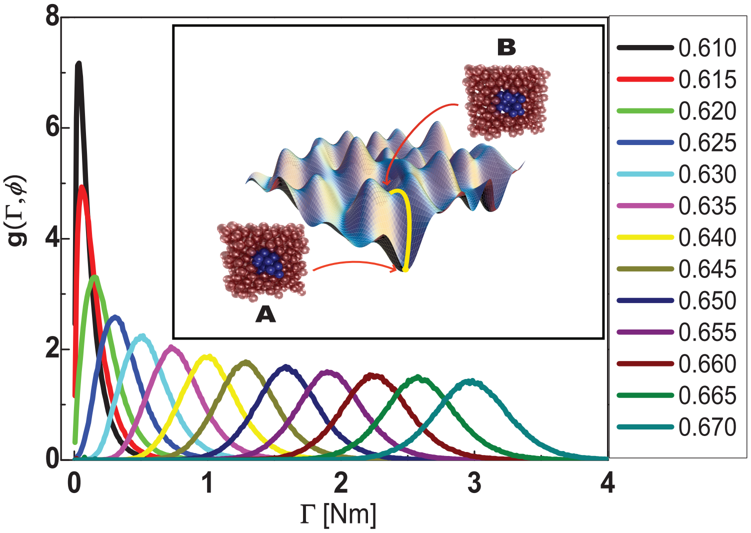

Figure 3.1: The density of states $g(\Gamma, \phi)$ as a function of internal virial Γ for different volume fraction, ϕ, ranging from 0.610 to 0.670. The inset is a schematic two-dimensional potential energy landscape surface. The jammed states A and B are local minima (zero order saddles) in the PES where the external force for each particle is zero and the Hessian matrix of the system is positive definite. Our simulation system consists of 30 frictionless spherical particles interacting by Hertzian forces with periodic boundary conditions.

peated cube [the interparticle potential energy is $E \propto (\delta r)^{\delta+1}$, see Supplementary Information-Section 3.3.1]. The Hertz potential is chosen for its general applicability to granular materials. The results are expected to be independent of the form of the potential. Details of the algorithms [16] to find the local minima of the PES (zero-order saddles) are in the Supplementary Information-Section 3.3.2. Figure 3.1 shows $g(\Gamma, \phi)$ versus Γ for different volume fractions.

3.2.2 MD Calculations

The pressure $\langle p \rangle_{\mathrm{dyn}}$ as a function of ϕ is calculated by performing MD simulations. Packings are prepared by compressing a gas of particles from an initial (unjammed) low volume fraction to a final jammed state. This procedure simulates a dynamical packing preparation [69]; details appear in Supplementary Information-Section 3.3.3. We obtain (Fig. 3.2a)

$$\langle p \rangle_{\mathrm{dyn}} = p_0 \ (\phi - \phi_c)^{1.65} \ , \tag{3.4}$$

where $\phi_c = 0.6077$ is the volume fraction corresponding to the isostatic point J [5] following Eq. (3.3) and $p_0 = 10.8$MPa. This critical value and the exponent, $a = 1.65$, are slightly different than the values obtained for larger systems ($a = \delta$)[5]. However, our purpose is to use the same system in the dynamical calculation and the exact enumeration for a proper comparison.

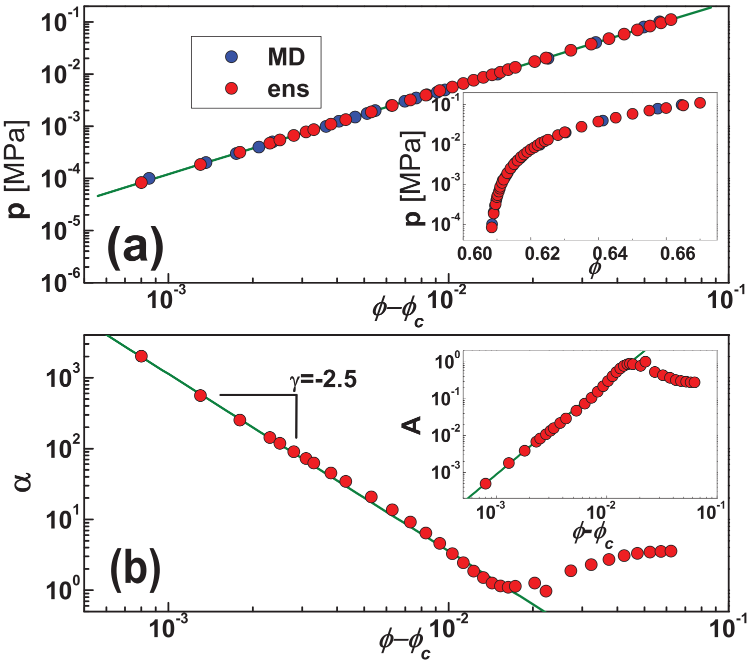

Figure 3.2: (a) The blue ◯ shows the power-law relation for $\langle p\rangle_{\mathrm{dyn}}$ vs $\langle\phi\rangle_{\mathrm{dyn}} - \phi_c$ for the 30-particle system. Here, the pressure $\langle p\rangle_{\mathrm{dyn}}$ are average values obtained by 250 independent MD simulations. The red ◯ is the pressure used to obtain the inverse angoricity α predicted by Eq. (3.4). The relatively small system size results in large fluctuations of the observables. In order to predict a precise relation for the system ($N = 30$), sufficient independent samples of the packings are generated to calculate the precise average for observables. We prepare 250 independent packings for each ϕ to get enough statistical samples to obtain $\langle p\rangle_{\mathrm{dyn}}$ and $\langle Z\rangle_{\mathrm{dyn}}$ by statistical average (see Supplementary Information-Fig. 3.13). The inset shows a semi-log plot. (b) The inverse angoricity α as a function of ϕ-ϕ_c. We find a power-law relation for system's volume fraction ϕ near ϕ_c. The solid line has a slope of -2.5. The inset is the angoricity $A(= 1/\alpha)$ vs ϕ-ϕ_c. To find A accurately for system's volume fraction ϕ much larger than ϕ_c, becomes difficult due to the large fluctuations and finite size effects. In principle, we may conjecture that the plateau of A for large volume fraction ϕ might be related to the finite size of the sample.

3.2.3 Angoricity Calculation

For each ϕ we use $g(\Gamma, \phi)$ to calculate $\langle p(\alpha)\rangle_{\text{ens}}$ by Eq. (3.1). Then, we obtain $\alpha(\phi)$ by setting $\langle p(\alpha, \phi)\rangle_{\text{ens}} = \langle p\rangle_{\text{dyn}}$ for every ϕ (see Supplementary Information-Figs. 3.14 and 3.15 and Supplementary Information-Section 3.3.4). The resulting equation of state $\alpha(\phi)$ is plotted in Fig. 3.2b and shows that the angoricity follows a power-law, near ϕ_c, of the form:

$$A \propto (\phi - \phi_c)^{\gamma}, \tag{3.5}$$

with $\gamma = 2.5$. The result is consistent with $\gamma = \delta + 1.0$, suggesting that $A \propto \Gamma \propto F_n r$. Angoricity is a measure of the number of ways the stress can be distributed in a given volume. Since the stresses have a unique solution for a given configuration at the isostatic point, ϕ_c, the corresponding angoricity vanishes. At higher pressure, the system is determined by multiple degrees of freedom satisfying mechanical equilibrium, leading to a higher stress temperature, A. The angoricity can also be viewed as a scale of stability for the system at different volume fractions. Systems jammed at larger volume fractions require higher angoricity (higher driving force) to rearrange.

3.2.4 Test of Ergodicity

In principle, using the inverse angoricity, α, from Eq. (3.5) we can calculate any macroscopic statistical observable $\langle B\rangle_{\text{ens}}$ at a given volume by performing the

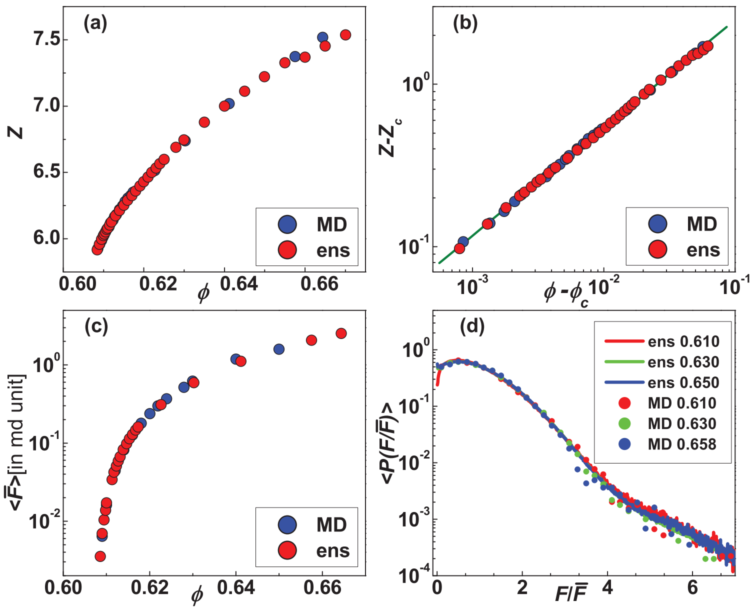

Figure 3.3: (a)The blue $\bigcirc$ is the average coordination number $\langle Z\rangle_{\rm dyn}$ obtained by 250 independent MD simulations. The red $\bigcirc$ is the coordination number $\langle Z\rangle_{\rm ens}$ calculated by the ensemble for different volume fractions. Agreement between both measures supports the concept of ergodicity in the system. (b)The same as (a) but in a log-log plot. The blue $\bigcirc$ shows the power-law relations for $\langle Z\rangle_{\rm dyn}$-$Z_c$ vs $\langle\phi\rangle_{\rm dyn}$ -ϕ_c for 30-particle system with $\phi_c = 0.6077$ and $Z_c = 5.82$. (c) Comparison of $\langle\overline{F}\rangle_{\rm dyn}$ and $\langle\overline{F}\rangle_{\rm ens}$ for different volume fractions. (d) The comparison of selected distribution of force $P_{\rm dyn}(F/\overline{F})$ and $P_{\rm ens}(F/\overline{F})$ for different volume fractions.

ensemble average [64]:

$$\langle B(\phi)\rangle_{\text{ens}} = \frac{1}{\mathcal{Z}} \int_0^\infty B\ g(\Gamma,\phi)\ e^{-\alpha\Gamma}\ \mathrm{d}\Gamma. \tag{3.6}$$

We test the ergodic hypothesis in the Edwards's ensemble by comparing Eq. (3.6) with the corresponding value obtained with MD simulations averaged over (250) sample packings, B_i, generated dynamically:

$$\langle B(\phi)\rangle_{\text{dyn}} = \frac{1}{250} \sum_{i=1}^{250} B_i. \tag{3.7}$$

The comparison is realized by measuring the average coordination number, $\langle Z\rangle$, the average force and the distribution of interparticle forces. We calculate $\langle Z\rangle_{\text{ens}}$ by Eq. (3.2) and $\langle Z\rangle_{\text{dyn}}$ as in Eq. (3.7). Figure 3.3a and 3.3b show that the two independent estimations of the coordination number agree very well: $\langle Z\rangle_{\text{ens}} = \langle Z\rangle_{\text{dyn}}$.

The average inter-particle force $\overline{F}$ for a jammed packing is proportional to the pressure of the packing. We calculate $\langle\overline{F}\rangle_{\text{ens}}$ and $\langle\overline{F}\rangle_{\text{dyn}}$ and find that they coincide very closely (see Fig. 3.3c). The full distribution of inter-particle forces for jammed systems is also an important observable which has been extensively studied in previous works [5, 70, 71]. The force distribution is calculated in the ensemble $P_{\text{ens}}(F/\overline{F})$ by averaging the force distribution for every configuration in the PES (see Supplementary Information-Section 3.3.5)). Figure 3.3d shows the distribution functions. The peak of the distribution shown in Fig. 3.3d indicates that the systems are jammed [5, 70, 71]. Besides the exact shape of the distribution, the similarity between the ensemble and the dynamical calculations shown in Fig.

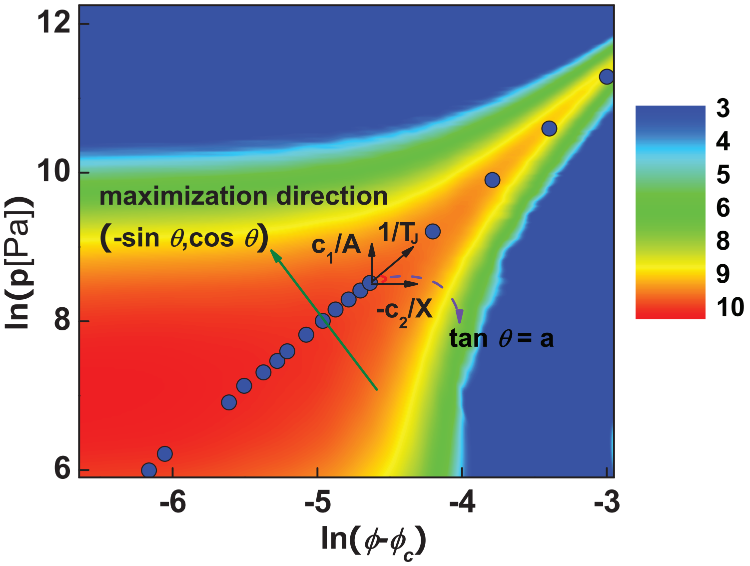

Figure 3.4: The entropy surface $S(\ln(\phi - \phi_c), \ln p)$. The color bar indicates the value of the entropy. The superimposed blue ◯ is $\langle p(\phi)\rangle_{\rm dyn}$ from MD calculations as in Fig. 3.2a. The olive arrow line indicates the maximization direction of the entropy $(-\sin\theta, \cos\theta)$. Following this direction, the entropy is maximum at the point $(\ln(\langle\phi\rangle_{\rm dyn} - \phi_c), \ln\langle p\rangle_{\rm dyn})$, corroborating the maximum entropy principle.

3.3d is significant. The study of $\langle Z\rangle$, $\langle\overline{F}\rangle$ and $P(F/\overline{F})$ reveals that the statistical ensemble can predict the macroscopic observables obtained in MD. We conclude that the idea of "thermalization" at an angoricity is able to describe the jamming system very well.

3.2.5 Thermodynamic analysis of the jamming transition

So far we have considered how the angoricity determines the pressure fluctuations in a jammed packing at a fixed ϕ. The role of the compactivity in the jamming transition can be analyzed in terms of the entropy which is easily calculated in the microcanonical ensemble from the density of states. Figure 3.4 shows $S = \ln(\Omega(p, \phi))$ (Ω is the number of states which is the unnormalized version of $g(\Gamma, \phi)$), which is the entropy of the system at the given (p, ϕ) in phase space.

We analyze the entropy surface $S(\ln(\phi - \phi_c), \ln p)$ plotted versus $(\ln(\phi - \phi_c), \ln p)$ in Fig. 3.4 and demonstrate that the MD curve $\langle p(\phi)\rangle_{\text{dyn}}$ passes along the maximum of the entropy surface constrained by the coupling between p and ϕ, Eq. (3.3) (such a curve is superimposed to the entropy surface in Fig. 3.4). Due to the coupling through the contact force law, the maximization of entropy is not on p or ϕ alone but on a combination of both. The entropy S reaches a maximum at the point $S(\ln(\langle\phi\rangle_{\text{dyn}} - \phi_c), \ln\langle p\rangle_{\text{dyn}})$ when we move along the direction perpendicular to the jamming curve $\langle p(\phi)\rangle_{\text{dyn}}$ (see the maximization direction in Fig. 3.4). This is a direct verification of the second-law of thermodynamics: the dynamical measures maximize the entropy of the system. We can use this result to obtain a relation between angoricity and compactivity. We write $\ln p = \ln p_0 + a\ln(\phi - \phi_c)$ where a is the exponent in Eq. (3.3), such that $S(\ln(\phi - \phi_c), \ln p)$ is maximized at the MD measures according to the direction of $(-\sin\theta, \cos\theta)$ ($\tan\theta = a$ is the slope of the power-law curve in the $\log - \log$ plot in Fig. 3.4). Therefore, neither A nor X can play the role of the temperature of the system alone, but a combination of both determined by entropy maximization satisfying the coupling between stress and strain. Since $\delta S = 0$ at $(\ln(\langle\phi\rangle_{\text{dyn}} - \phi_c), \ln\langle p\rangle_{\text{dyn}})$ along $(-\sin\theta, \cos\theta)$ then $(\partial S/\partial \ln p)\cos\theta - (\partial S/\partial \ln(\phi - \phi_c))\sin\theta = 0$. We obtain $c_1\alpha + ac_2\beta = 0$ (where $c_1 = \Gamma$ and $c_2 = (\phi - \phi_c)(NV_g/\phi^2)$) and the relation between A and X (see Supplementary Information-Fig. 3.20 and Supplementary Information-Section 3.3.6):

$$X = -aA(\phi - \phi_c)/p\phi. \tag{3.8}$$

From Eq. (3.8) we obtain that: $X \propto -(\phi - \phi_c)^{1+a-\gamma}/\phi$ and near ϕ_c:

$$X \sim -(\phi - \phi_c)^2. \tag{3.9}$$

We notice that the compactivity is negative near the jamming transition. A negative temperature is a general property of systems with bounded energy like spins [54]: the system attains the larger volume (or energy in spins) at ϕ_c when $X \to 0^-$ and not $X \to +\infty$ [The bounds $\phi_c \leq \phi \leq 1$ imply that the jamming point at $X \to 0^-$ is "hotter" than $X \to +\infty$. At the same time $A \to 0^+$ since the pressure vanishes].

We conclude that, A and X alone cannot play the role of temperature. Instead, there is an actual "jamming temperature" $T_{\rm J}$ that determines the direction $(-\sin\theta, \cos\theta)$ in the $\log-\log$ plot of Fig. 3.4 along the jamming equation of state (see Supplementary Information-Fig. 3.20). By maximizing the entropy along this direction we obtain $T_{\rm J}$ as a function of A and X (see Supplementary Information-Section 3.3.6):

$$T_{\rm J} = \sin\theta \frac{A}{\Gamma} = \frac{a}{\sqrt{1+a^2}}\frac{A}{\Gamma} \sim (\phi - \phi_c)^{\gamma - a}. \tag{3.10}$$

By the definition of "heat" capacity, we obtain two jamming capacities as the response to changes in A and X:

$$C_\Gamma \equiv \partial\Gamma/\partial A \sim (\phi - \phi_c)^{-1} \sim A^{-2/5}, \text{ and } C_{\rm V} \equiv \partial V/\partial X \sim (\phi - \phi_c)^{-1} \sim |X|^{-1/2}. \tag{3.11}$$

From Eq. (3.11), the jamming capacities diverge at the jamming transition as $A \to 0^+$ and $X \to 0^-$. However, this result does not imply that the transition is critical since from fluctuation theory of pressure and volume [54] we obtain:

$$\langle(\Delta\Gamma)^2\rangle = A^2 C_\Gamma \sim A^{1.6}, \quad \text{and} \quad \langle(\Delta V)^2\rangle = X^2 C_\mathrm{V} \sim |X|^{1.5}. \qquad (3.12)$$

Thus, the pressure and volume fluctuations near the jamming transition do not diverge, but instead vanish as $A \to 0^+$ and $X \to 0^-$. From a thermodynamical point of view, the transition is not of second order due to the lack of critical fluctuations. As a consequence, no diverging static correlation length can be found at the jamming point. However, other correlation lengths of dynamic origin may still exist in the response of the jammed system to perturbations, such as those imposed by a shear strain or in vibrating modes [62, 72]. Such a dynamic correlation length would not appear in a purely thermodynamic static treatment as developed here. We note though that responses to shear can be treated in the present formalism by allowing the inverse angoricity to be tensorial [64]. The intensive jamming temperature Eq. (3.10) gives use to a jamming effective energy E_J as the extensive variable satisfying $T_\mathrm{J} = \partial E_\mathrm{J}/\partial S$ and a full jamming capacity $C_\mathrm{J} \sim (\phi - \phi_c)^{-1}$, which also diverges at jamming (see Supplementary Information-Section 3.3.6). However, the fluctuations of E_J defined as $\langle(\Delta E_\mathrm{J})^2\rangle = T_\mathrm{J}^2 C_\mathrm{J} \sim T_\mathrm{J}$ has the same behavior as the fluctuations of volume and pressure, vanishing at the jamming transition $T_\mathrm{J} \to 0^+$ [$A \to 0^+$ in Eq. (3.10)].

3.2.6 Comparison with O'Hern *et al.*

We now turn to a comparison of our results with similar simulations done by O'Hern *et al.* [65, 73]. O'Hern *et al.* performed an exhaustive search of all configurations in the PEL of frictionless particles similarly as done in the present paper. However, they find that the microstates are not equiprobable, i.e., microstates with the same pressure and volume fraction (pressure is fixed at zero in [65, 73] since only hard sphere states are of interest) do not have the same probability when sampled by a given algorithm. Furthermore, experimental studies of equilibration between two systems [74] suggests that a hidden variable is necessary to describe the microstates, further supporting the results of [73].

The applicability of the microcanonical ensemble is based on the fact that the microstates are defined by (Γ, ϕ). Thus, the fact that the states are not equiprobable implies that there must be an extra variable needed to describe their probabilities. Therefore, ergodicity and the maximum entropy principle, which are downstream from equiprobability, are not supposed to hold, in disagreement with the results shown in the present paper.

To investigate this conundrum, we repeat the same calculations as in [73] with our algorithms. We first rule out subtleties related to algorithmic dependent results in sampling the space of configurations. We use our 30 particles system and use $\phi = 0.61$ very close to jamming and $\Gamma = 0$ to look for the hard sphere packings. We search for the jammed configurations as above. We recall that the sampling of the space of configurations is not complete due to the relatively large number of particles ($N = 30$) but represents a good sampling as discussed above. Ref. [73] uses a different system of 14 particles in 2d for which 248,900 configurations are found exhaustively sampling the phase space (which is estimated to have $\sim 371,500$ states). Our simulations correspond to a system with periodic boundary conditions for which a larger space is expected than the close boundary-system. We use

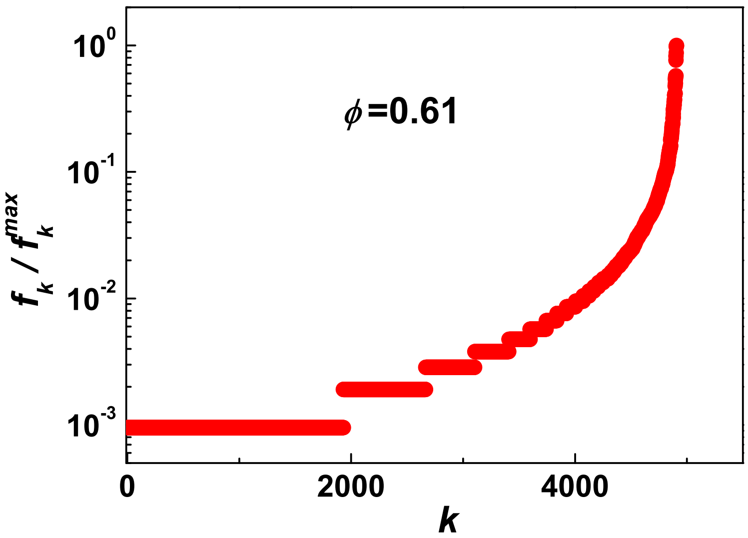

Figure 3.5: Sampling probability of each microstate f_k identified by its rank k from low to high. Results are for a system of 30 particles at $\phi = 0.61$ and a narrow set of pressures around 0. We calculate only a sample of the configurations.

$N = 30$ in $3d$ and find $\sim 1.5 \times 10^6$ configurations for a given ϕ and for all Γ (including the hard-sphere states $\Gamma = 0$) which does not represent all the states but saturates the density of states. However, these differences do not affect the conclusions below.

We start by measuring f_k which is the probability to find a given microstate labeled k as defined by [73]: each packing can be obtained many times during a search using a particular protocol. Therefore, f_k measures the probability for which each packing occurs. This probability is dependent on the protocol used, and, in principle, does not reflect the probabilities that the system will access during a typical experiment. We sort the microstates in order ok increasing probability f_k such that k measures the rank of the state, $k = 1, ..., k_{\max}$, where $k_{\max}$ is the total number of states at this particular (Γ, ϕ). The main result of [73] is that f_k differs by many orders of magnitude for states with fixed (Γ, ϕ). Indeed, even configurations which are visually very similar can be 10^6 more frequent, see Fig. 1 of [73].

Figure 3.5 shows f_k sorted as a function of the rank k as in [73] for a system at $\phi = 0.61$ and a narrow set of pressures around $\Gamma = 0$. We calculate only a sample of the configurations. This plot reproduces the results of O'Hern *et al.* [73] within our system. For a fixed pressure and volume there are many states with a large difference in their probability. The least probable states represents almost 40% of the total and are 10^{-3} less probable than the most probable states showing a breakdown of equiprobability. The question is how to interpret the results of ergodicity in the light of the nonuniform distribution f_k, and whether there is a need for an extra variable to describe the microstates:

(i) Firstly, we point out the standard interpretation of the flat average. The uneven distribution f_k was obtained here by a particular protocol, the greedy LBFGS search. The nonuniform distribution of configurations f_k does not enter in the ensemble formalism, since all the states k are taken as equally probable. We use only the information on the total number of configurations, $k_{\max}$, to compute the density of states $g(\Gamma, \phi)$ for a given (Γ, ϕ). Clearly, the greedy LBFGS search is a particular convenient protocol to obtain all the configurations in the PEL that bears no resemblance with the real dynamics of the system, which is, for instance, obtained in a typical shaking experiment *a la* Chicago. Thus, the probabilities f_k are not physical observables and a different protocol will give a different f_k, albeit with the same number of total configurations, $k_{\max}$, as long as it is run long enough. For instance, in our protocol we have used MC at high temperature to find initial configurations to apply the greedy search. But we could have used MD at finite

temperature and the probability of each state could have been different, although the final number k_{max} would be the same if the protocol is run long enough.

In agreement with this, the ensemble averages of pressure and others variables cannot be obtained directly from f_k. Once the configurations are enumerated, the density of states can be computed. Then the observables are obtained as a function of A in the proper Boltzmann distribution. The use of the flat assumption can only be tested a posteriori in the comparison between the dynamical measures and the ensemble average, as stated by the ergodic principle.

Therefore, from a conceptual point of view, there is no physical contradiction between the nonuniform f_k and the flat average assumption in Statistical Mechanics: f_k is a purely protocol-dependent estimate with no physical meaning. Perhaps, a better estimation of f_k should be obtained over many protocols which could then give a flat behavior.

The long and the short of it, the probabilities f_k are protocol dependent features and do not enter in the physical average of the observables. The low probability states that are generated by the Greedy LBFGS protocol may become highly probable if we change the protocol. It may well be that different protocols explore different regions of the phase space. The important issue is to obtain the total number of states, k_{max}, which is independent on the probability that every protocol use to access the states. The fact that different Greedy protocols sample differently the configurational spaces does not disproved a thermodynamics treatment.

Another issue is whether a realistic MD protocol that simulates the shaking reversible states in the Chicago experiments could visit a restricted region of the phase space. This situation carries no conflict as well, as long as the configurations are the typical ones in the $\exp\left[-\alpha\Gamma\right]$ ensemble, that is, as long as ergodicity works. Yet another issue is whether different protocols such as the Lubachevsky-Stillinger (LS) algorithm [75], the Jodrey-Tory algorithm (JT) [76] or our own split-algorithm with MD used here access different states with different volume fractions. There is no conceptual problem either; these different preparations may "thermalize" the packings at different compactivities; we are treating athermal systems and we have no benefit of an equilibrium temperature to sample the space of states.

For instance, we recently studied hard-sphere packings from volume fractions spanning from random loose packings, RLP on the lower end of volume fractions $\phi \sim 0.54$, to FCC at $\phi = 0.74$ using the three different protocols above [77]. We find that the LS algorithm [75], the JT algorithm [76] and our MD give rise to different volume fraction regions, although with large overlaps. When the Edwards statistic mechanics is applied to all these packings, a unifying thermodynamic picture emerges, independent of protocols.

However, we should not dismiss the finding on the uneven f_k for a given protocol since they are surprisingly robust and they must relate to fundamental properties of the PEL or some hidden symmetries of the packings. We investigate these issues next.

(ii) Second, we mention the issue of the small system size. It is quite possible that the low probability states will completely disappear in the thermodynamic limit. This "incredible lucky scenario" will allow the most probable configurations to remain, then, with equal probability. Indeed, the flat average assumption is only valid in the thermodynamic limit and simply states that, even if there are less probable states (10^{-3} less probable), they are irrelevant in the ensemble average;

only the most-probable and equiprobable states are relevant in the thermodynamic limit. Comparing our simulations with larger system size than $N = 30$ may resolve the non-equiprobability problem. However, calculations for larger systems to test this assertion are out of the range of current and near future computational power.

(iii) Finally, nonuniform f_k might be related to some property of the topology of the energy landscape which is captured by the particular algorithm used to sample it. To investigate this point, we construct the network of configurations [23] (Fig. 3.6a) of a 14-particle system of Hertz spheres at volume fraction $\phi = 0.64$ based on the LBFGS search of minima and eigenvector following method to calculate the saddle points. A node in the network is a jammed configuration and a link connects two nodes if the corresponding configurations are connected through a saddle point in the PEL. For this calculation we use a smaller system size since the finding of all the transition states is very time consuming and not feasible for $N = 30$. The resulting network contains all the states with possible Γ for the given ϕ and not only the hard-sphere states, $\Gamma = 0$, used in [73].

As we show in Fig. 3.6b, the degree n_k (number of neighboring jammed states connected through first-order saddle) of a jammed state in the PEL-network is relatively well correlated with the probability f_k. The larger n_k, the larger the probability that the state will be visited. We note the large span in the number of connections of the microstates. Indeed, the network of jammed states has a broad distribution of links as the LJ network studied by Doye. This raises a reasonable explanation of the uneven probability, which could be rooted in the inhomogeneous degree distribution of Fig. 3.6b, which again leave us a mystery for future investigations. Furthermore, since the initial MC unjammed configuration

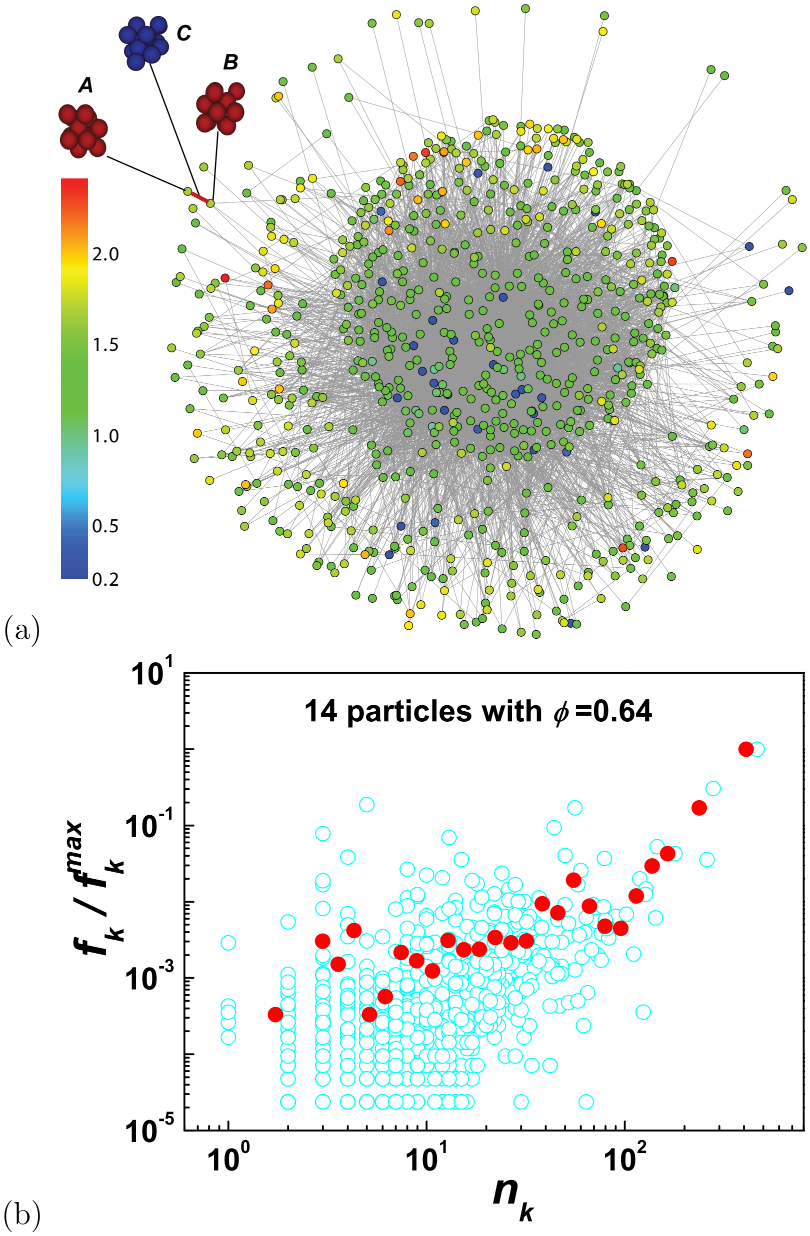

Figure 3.6: (a) The network of a Hertz 14-particle system with volume fraction $\phi = 0.64$. A node in the network is a jammed configurations and a link connects two nodes if the corresponding configurations are connected through a saddle point in the PEL. For example, nodes A and B are two packings as depicted connected through a saddle C, red bond in the plot. Different color in the plot indicates different Γ of the node. (b) The cyan ◯ is the probability f_k for each jammed state with degree n_k in the network formed by jammed configurations linked by first-order saddles. n_k is the number of links in the network for a given configuration k. The red ◯ is the average probability $\langle f_k \rangle$ for jammed states with the average degree $\langle n_k \rangle$. Following the red points, it seems that f_k are correlated with n_k.

is in the basin of attraction of a jammed state which is then obtained under LBFGS search, the uneven distribution is surely reflecting a very nonuniform size of the basins of attraction surrounding each potential energy minimum microstate in the PEL.

3.2.7 Conclusion

We have demonstrated that the concept of " thermalization " at a compactivity and angoricity in jammed systems is reasonable by the direct test of ergodicity. The numerical results indicate that the full canonical ensemble of pressure and volume describes the observables near the jamming transition quite well. From a static thermodynamic viewpoint, the jamming phase transition does not present critical fluctuations characteristic of second-order transitions since the fluctuations of several observables vanish approaching jamming. The lack of critical fluctuations is respect to the angoricity and compactivity in the jammed phase $\phi \to \phi_c^+$, which does not preclude the existence of critical fluctuations when accounting for the full range of fluctuations in the liquid to jammed transition below ϕ_c. Thus, a critical diverging length scale might still appear as $\phi \to \phi_c^-$ [78], which has been recently observed by experiment [79]. In conclusion, our results open the door to an ensemble treatment of the jamming transition. One possible analytical route to use this formalism would be to incorporate the coupling between volume and coordination number at the particle level found in [66] together with similar dependance for the stress to solve the partition function. This treatment would allow analytical solutions for the observables with the goal of characterizing the scaling law near the jamming transition.

3.3 Supplementary Information

3.3.1 System Information

The systems used for both, ensemble generation and molecular dynamic simulation, are the same. They are composed of 30 spherical particles in a periodic boundary box. The particles have same radius $r = 5\mu m$ and interact via a Hertz normal repulsive force without friction. The interaction is defined as:

$$F_n = \frac{2}{3}\, k_n r^{1/2}(\delta r)^{1.5}, \tag{3.13}$$

where $\delta r = (1/2)[2r - |\vec{x}_1 - \vec{x}_2|] > 0$ is the normal overlap and $k_n = 4G/(1-\nu)$ is defined in terms of the shear modulus G and the Poisson's ratio ν of the material from which the grains are made. Here, we use $G = 29$ GPa and $\nu = 0.2$ for spherical particles and the density of the particles, $\rho = 2 \times 10^3$ kg/m^3.

3.3.2 Ensemble Generation

In this section, we first explain the method to obtain geometrically distinct minima in the PEL. Then we show that the density of the states, $g(\Gamma, \phi)$, does not change significantly after sufficient searching time for the configurations.

For N structureless particles possessing no internal orientational and vibrational degrees of freedom, at a fixed volume fraction ϕ, the potential energy is a $3N-$dimensional function, $E(r_1, \ldots, r_N)$, depending on the positions r_i of the N particles. In principle, if all local minima corresponding to the mechanically stable configurations of the PEL are obtained, the density of states $g(\Gamma, \phi)$ can be calculated. Such an exhaustive enumeration of all the jammed states requires that N not be too large due to computational limits. On the other hand, in order to obtain a precise average pressure in the MD simulation, $\langle p\rangle_{\mathrm{dyn}}$, N cannot be too small such that boundary effects are minimized. Considering these constraints, we choose a 30 particle system.

In order to enumerate all the jammed states at a given volume fraction ϕ, we start by generating initial unjammed packings (not mechanically stable) performing a Monte Carlo (MC) simulation at a high, fixed temperature. The MC part of the method applied to the initial packings assumes a flat exploration of the whole PEL. Every MC unjammed configuration is in the basin of attraction of a jammed state which is defined as a local minimum in the PES with a positive definite Hessian matrix, that is a zero-order saddle. In order to find such a minimum, we apply the LBFGS algorithm provided by Nocedal and Liu [16]. The procedure is analogous to finding the inherent structures [23] of glassy systems. The LBFGS algorithm is also similar to the conjugate gradient method employed by O'hern [5, 65], but it is computationally more efficient since it does not require the calculation of the Hessian matrix of the system at any time step. The PEL for each fixed ϕ likely includes millions of geometrically distinct minima by our simulation results. Therefore, an exhaustive search of configurations is computationally long. We check that the number of found configurations has saturated after sufficient trials and that the density of states $g(\Gamma, \phi)$ has converged to a final shape.

It is also important to determine if the local minima are distinct. Usually, the eigenvalues of the Hessian matrix at each local minimum can be used to distinguish these mechanically stable packings. Here, we follow this idea to compare minima to filter the symmetric packings. However, instead of calculating the eigenvalues of each packing, which is very time consuming, we calculate a function of the distance between any two particles in the packing to improve search efficiency (for the LBFGS algorithm, we do not need to calculate the Hessian matrix). For each packing, we assign the function Q_i for each particle in the system:

$$Q_i = \sum_{1\leq j\leq N,\ \ j\neq i} \tan^2(\frac{\pi r_{ij}^2}{3L^2}), \tag{3.14}$$

where r_{ij} is the distance between particles i and j, L is the system size and $N = 30$ is the number of the particles of the system. We list the Q_i for each packing from minimum to maximum $\{Q_i\}(0 < i \leq N)$. Since Q_i is a higher order nonlinear function, we can assume that two packings are the same if they have the same list. The tolerance is defined as:

$$T = \sqrt{\frac{\sum_{1\leq i\leq N}(Q_i - Q_i^{'})^2}{N^2}}, \tag{3.15}$$

where Q_i and $Q_i^{'}$ are the corresponding values from the lists of two packings.

Figure 3.7 shows the distributions of the tolerance T for packings at different volume fractions. This figure suggests that two packings can be considered the same if $T \leq 10^{-1}$, which defines the noise level.

We are now ready to calculate $g(\Gamma, \phi)$ from the number of jammed configurations as a function of Γ for a system with fixed ϕ. Figure 3.8 investigates the convergence of $g(\Gamma, \phi)$ for three values of ϕ, as more configurations are found with the LBFGS algorithm. From Fig. 3.8(a), (b), (c), we see that $g(\Gamma, \phi)$ does not change significantly and have converged well to a final state after $\sim$ 1.4 million

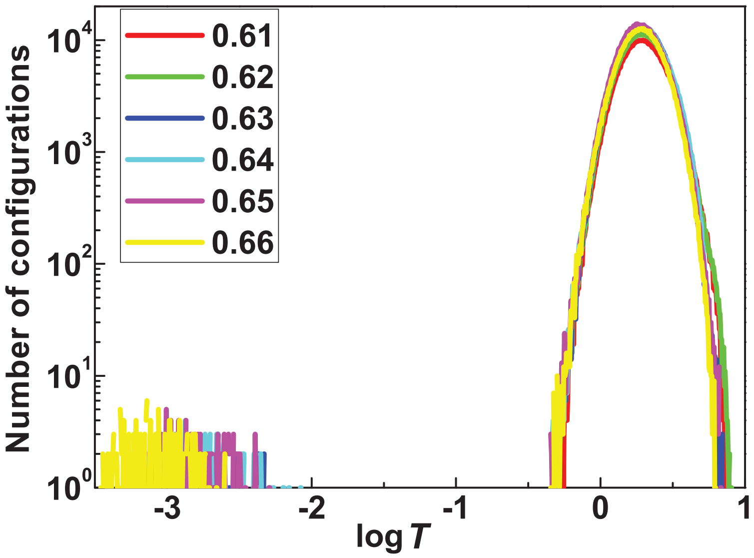

Figure 3.7: The distribution of the tolerance T between any two packings at the given ϕ. From the graph, the value of T for which any two different packings are considered to be same is chosen to be 10^{-1}, which is above the noise threshold and below the distribution of T.

configurations have been found. We also plot the number of new states found in the i-th day of running the code, $N_{\text{new}}(i)$, versus the total number of found configurations up to the i-th day of computer search, $N_{\text{total}}(i)$. We run the search for 15 days and obtain a maximum of $\sim 1.4\times10^6$ configurations for each ϕ. Notice that these configurations span all possible accessible values of pressure.

Figure 3.9 plots the probability of finding new configurations, $N_{\text{new}}(i)/N_{\text{total}}(i)$, versus $N_{\text{total}}(i)$ for different volume fractions suggesting that $N_{\text{new}}(i)/N_{\text{total}}(i)$ has converged in the linear plot. However, the log-log plot of the inset in Fig. 3.9 indicates that the algorithm is still searching for new configurations; the power-law relation in the inset suggests a neverending story. However, the main point is whether the observables have converged and not whether we have obtained all the configurations. According to Fig. 3.8, $g(\Gamma,\phi)$ has already converged to a final form

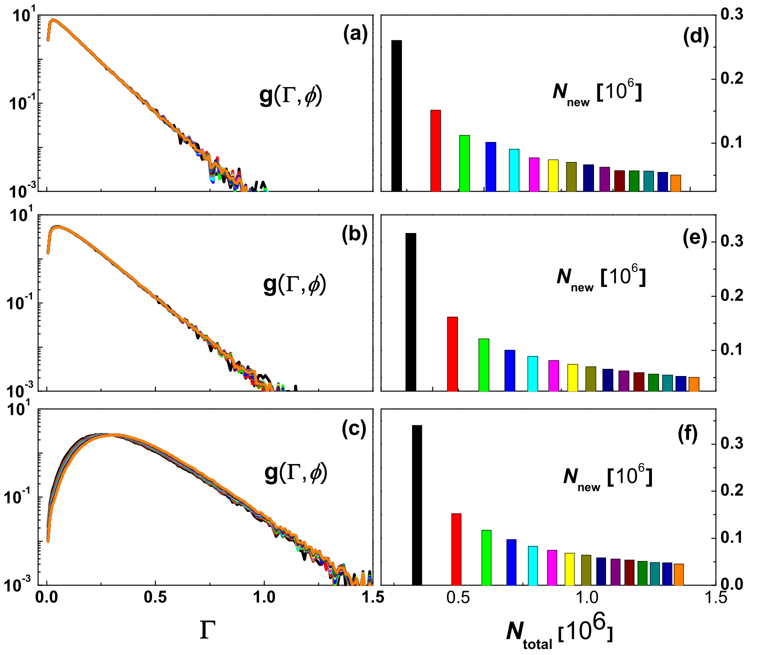

Figure 3.8: Log-log plot of the density of states $g(\Gamma, \phi)$ (a) at $\phi = 0.609$, (b) at $\phi = 0.614$, (c) at $\phi = 0.625$. Different color in (a), (b), (c) corresponds to the different number of configurations plot in (d),(e),(f) with the same color column bar. We find that the distributions have converged after locating enough number of configurations.

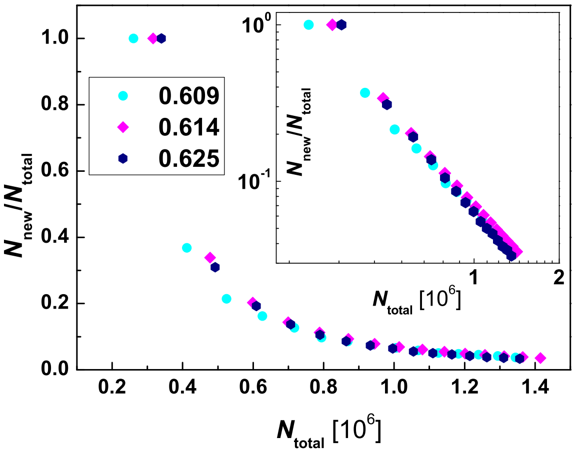

Figure 3.9: The probability to find new configurations as a function of searching time measured in the total number of obtained configurations. The inset is a log-log plot.

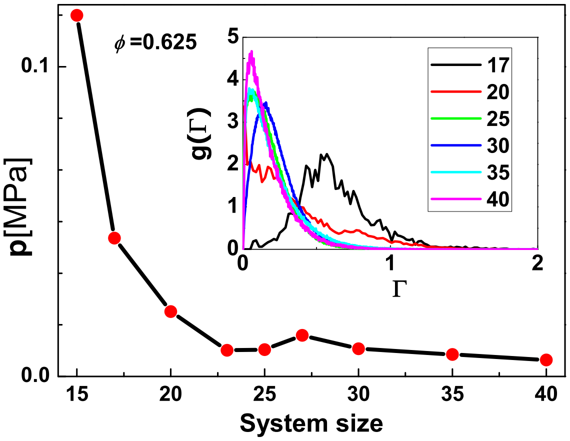

Figure 3.10: Dependence of the results on the system size. The average value of p converges as early as $N \sim 25$ particles. The distribution $g(\Gamma, \phi)$ (inset) has not fully converged yet but its shape has converged after $N = 35$ and the first moment does not change as indicated by the average p.

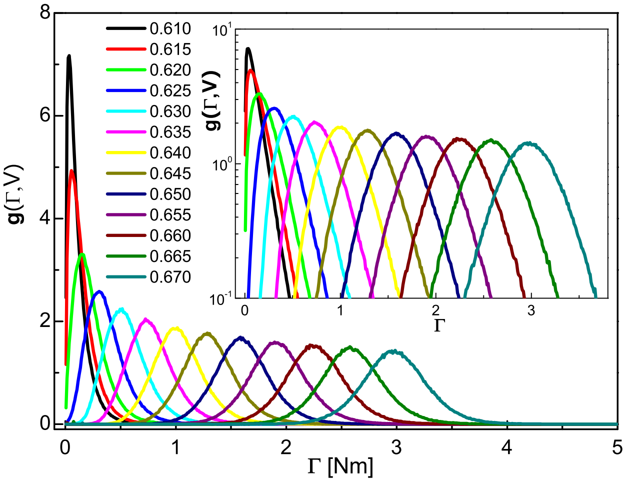

Figure 3.11: The density of states $g(\Gamma, \phi)$ as a function of internal virial Γ for different volume fraction, ϕ, ranging from 0.610 to 0.670. The inset shows the logarithmic distribution of $g(\Gamma, \phi)$.

after we found more than a million of configurations even though $N_{\text{new}}(i)/N_{\text{total}}(i)$ is still finite. A further test of convergence supporting this point is obtained below in Fig. 3.16 where the value of the inverse angoricity is measured as a function of the searching time measured in $N_{\text{total}}(i)$. This plot suggests that enough ensemble packings have been obtained to capture the features of $g(\Gamma, \phi)$ that give rise to the correct observables. We conclude that we have obtained an accurate enough density of states for this particular system size even though we have not found all configurations.

Regarding system size dependence, the presented results are still N dependent, although they started to converge for $N \sim 35$ and above according to Fig. 3.10. More accurate calculations for large values of N remain computationally impossible. However, we note that in our treatment the exact choice of N is not as important as the consistency of the results between ensemble and MD for a given N value.

Figure 3.11 shows $g(\Gamma, \phi)$ versus Γ for all volume fractions considered in this study. At low volume fraction ($\phi \lesssim 0.625$), the distributions are sharp and the tails of the distributions are exponential. At high volume fraction ($\phi \gtrsim 0.640$), the distributions are much broader and the tails are Gaussian.

3.3.3 MD Generation

In order to analyze numerical results, we perform MD simulations to obtain Z_{dyn}, ϕ_{dyn} and ϕ_{dyn}, which are herein considered real dynamics.

The preparation protocol consists of first preparing a gas of non-interacting particles at an initial volume fraction ϕ_i in a periodically repeated cubic box. The particles do not interact and are randomly generated, usually with a volume fraction $\phi_0 \approx 0.30 \sim 0.36$, then an extremely slow isotropic compression is applied on this dilute configuration until the system reaches another unjammed configuration at higher density, ϕ_i. The reason to add an extremely slow isotropic compression to the dilute configuration is to avoid involving any kinetic energy to keep the system as random as possible. After obtaining this unjammed state with initial volume fraction ϕ_i, a new compression is applied with a compression rate Γ ($\Gamma_0 = 5.9 t_0^{-1}$, where the time is in units of $t_0 = R\sqrt{\rho/G}$.) until the pressure p_1 is a slightly higher than the prefixed pressure we choose. Then the compression is stopped and the system is allowed to relax to mechanical equilibrium by following Newton's equations without further compression.

After the compression to p_1, two things can occur (see Fig. 3.12):

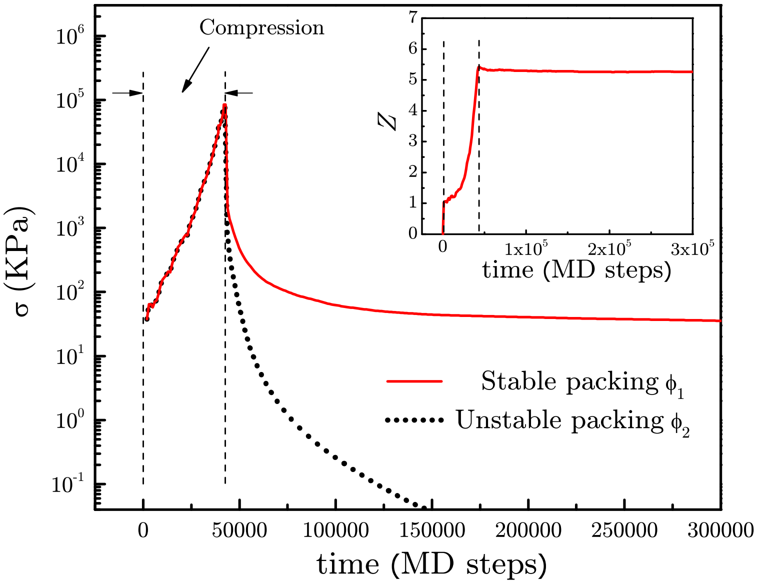

Figure 3.12: Time evolution of stress (the pressure in the system) for two packings simulated as explained in the text. The solid red line represents a packing with $\phi_1 > \phi_c$ and dotted black line represents a packing with $\phi_2 < \phi_c$, where $\phi_1 = \phi_2 + 2 \times 10^{-4}$. The inset shows the time evolution of the coordination number.

(a) The system jams: If the system is above the jamming point $\phi_1 > \phi_c$, then the stress will decrease and ultimately stabilize to a finite nonzero value, meaning that the pressure of the system remains unchanged (usually $\Delta\sigma < 10^{-3}$ Pa, red line, Fig 3.12) over a large period of time (usually $\sim 10^7$ MD steps). The coordination number usually has a first initial decrease, but if the system is jammed it will also stabilize at a constant value above the isostatic minimal number (inset Fig. 3.12).

(b) The system is not jammed: here the stress and the coordination number will relax to zero. This fact is illustrated in Fig. 3.12. If the packing has $\phi_1 > \phi_c$, it stabilizes at a non-zero pressure above the jamming transition, but the pressure decreases very quickly to zero (the system is not jammed) if $\phi_2 < \phi_c$, even though ϕ_1 and ϕ_2 differ only by 2×10^{-4}.

Then the system is compressed and relaxed repeatedly until the system can be mechanically stable at the predetermined pressure. It is important to determine whether the packings are jammed in the sense that they are not only mechanically stable but also they are stable under perturbations. Numerical protocols herein assure that the system is at least locally jammed since each particle is in mechanical equilibrium [80]. To test if the system is collectively jammed is more involved. For frictionless systems, where tangential forces are removed, the Hertz energy $U_{\rm hertz} = \frac{4}{15}\, k_n R^{1/2}\delta^{5/2}$ is used to test whether the Hessian of the jammed configurations is positive. The frictionless configurations have positive Hessian indicating that they are collectively jammed. Here the compression rate is $\Gamma_0 = 5.9 t_0^{-1}$, where the time is in units of $t_0 = R\sqrt{\rho/G}$. To obtain the statical average of $Z_{\rm dyn}$ and $\phi_{\rm dyn}$, we repeat the simulation to get enough packing samples having statistically independent random initial particle positions. Here, 250 independent packings are obtained for each fixed pressure (see Fig. 3.13). $\phi = \langle\phi\rangle_{\rm dyn}$ and $\langle Z\rangle_{\rm dyn}$ are flat averages of these 250 packings by $\langle\phi\rangle_{\rm dyn} = \frac{\sum_{1\leq i\leq 250}\phi_i}{250}$ and $\langle Z\rangle_{\rm dyn} = \frac{\sum_{1\leq i\leq 250} Z_i}{250}$.

3.3.4 Angoricity Calculation

Since we obtain $g(\Gamma,\phi)$ and $\langle p\rangle_{\rm dyn}$ for each volume fraction ϕ, we can calculate the inverse angoricity α by Eq. (3.1). The pressure $\langle p(\alpha,\phi)\rangle_{\rm ens}$ for a given ϕ is a function depending on α as:

$$\langle p(\alpha,\phi)\rangle_{\rm ens} = \frac{\int_0^\infty p g(\Gamma,\phi) e^{-\alpha\Gamma} {\rm d}\Gamma}{\int_0^\infty g(\Gamma,\phi) e^{-\alpha\Gamma} {\rm d}\Gamma} = \frac{\sum p e^{-\alpha\Gamma}}{\sum e^{-\alpha\Gamma}}. \tag{3.16}$$

Figure 3.14 shows the result of the numerical integration of Eq. (3.16) for a

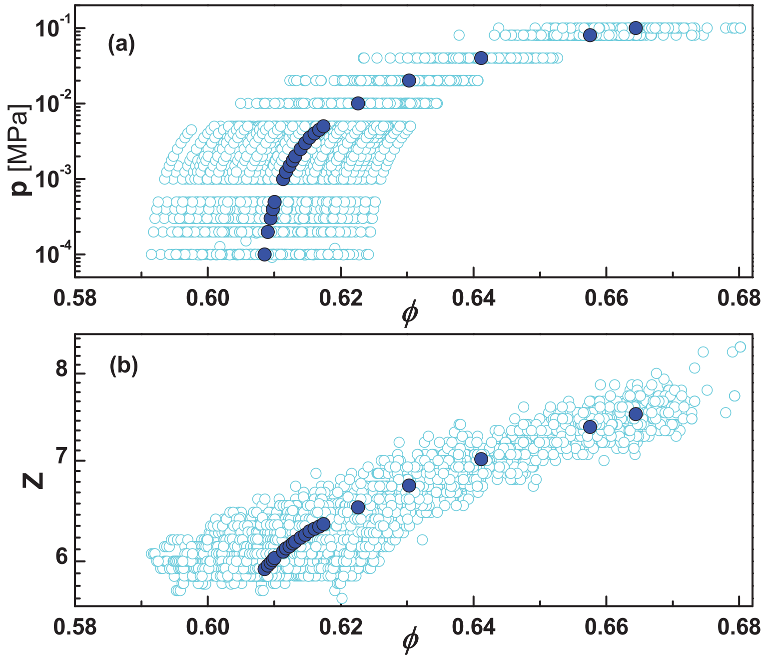

Figure 3.13: The cyan ◯ is Z_{dyn} and ϕ_{dyn} for every single packing obtained with MD and the blue ◯ is $\langle\phi\rangle_{\mathrm{dyn}}$ and $\langle Z\rangle_{\mathrm{dyn}}$ average over the single packings for the system which are shown in the main text of the paper.

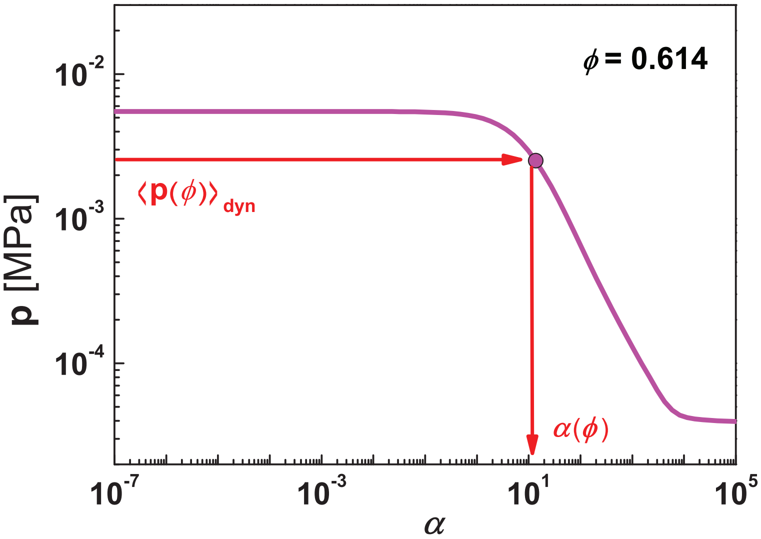

Figure 3.14: The numerical integration of Eq. (3.16) for $\phi = 0.614$ is shown as the pink curve. We input the $\langle p\rangle_{\mathrm{dyn}}$ (pink ◯ in the plot) and obtain the corresponding inverse angoricity α.

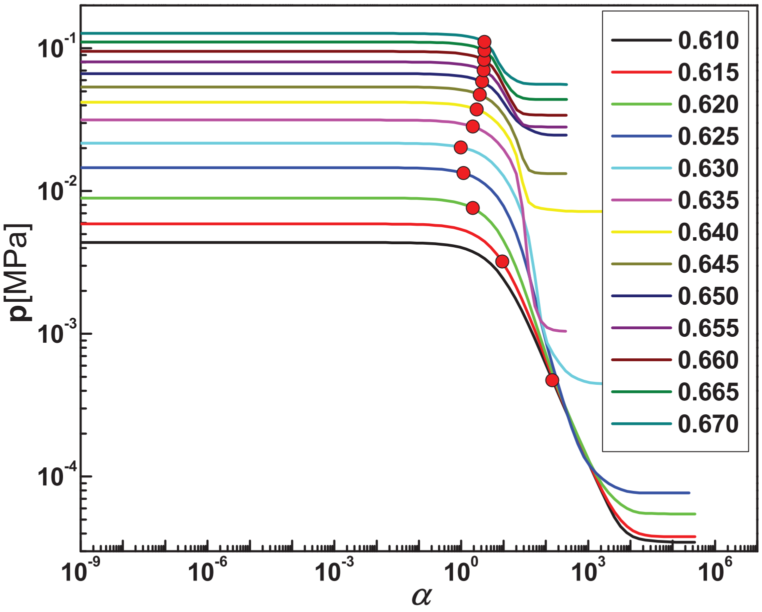

Figure 3.15: Calculation of α for several volume fractions ϕ as explained in detail in Fig. 3.14

particular $\phi = 0.614$ as a function of α using the numerically obtained $g(\Gamma, \phi)$ from Fig. 3.1. To obtain the value of α for this ϕ, we input the corresponding measure of the pressure obtained dynamically $\langle p(\phi)\rangle_{\rm dyn}$ and obtain the value of α as schematically depicted in Fig. 3.14. The same procedure is followed for every ϕ (see Fig. 3.15) and the dependence $\alpha(\phi)$ is obtained. The result is shown in Fig. 3.2(b) in the main text.

We also check the inverse angoricity $\alpha(\phi)$ using $g(\Gamma, \phi)$ for different number of total configurations $N_{\rm total}$ to ensure the accuracy and convergence to the proper value. From Fig. 3.16, we can see that, $\alpha(\phi)$ is stable due to the fact that the density of state, $g(\Gamma, \phi)$, does not change significantly after $N_{\rm total}$ is above 10^6 configurations.

For volume fraction much larger than ϕ_c, the system's input pressure $\langle p(\phi)\rangle_{\rm dyn}$

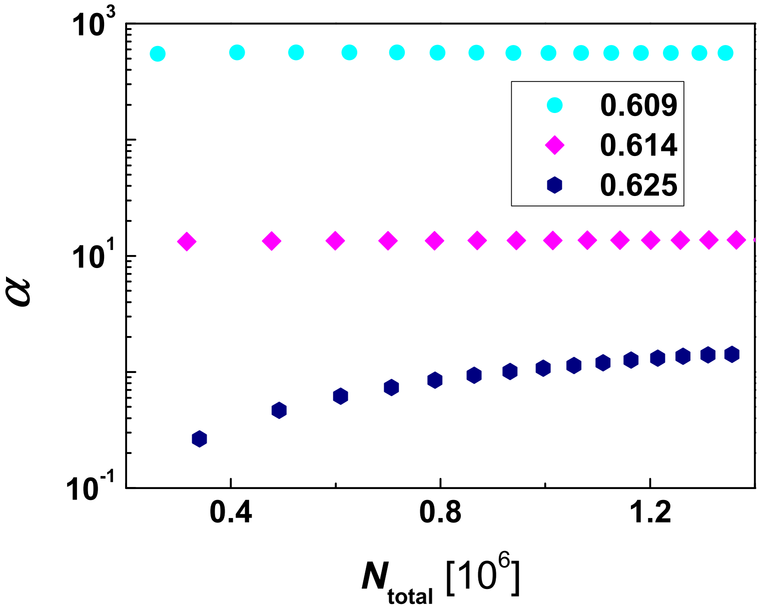

Figure 3.16: Calculation of inverse angoricity α as a function of N_{total}.

reaches the plateau at low α of the function $\langle p(\alpha,\phi)\rangle_{\text{ens}}$ (see Fig. 3.15) and the corresponding $\alpha(\phi)$ becomes much smaller (the angoricity $A(\phi)$ becomes much larger), leading to large errors in the value of A as ϕ becomes large. This might explain the plateau found in A when $(\phi - \phi_c) > 2 \times 10^{-2}$ as shown in Fig. 3.2b.

Using $\alpha(\phi)$ for each volume fraction, we calculate $\langle Z\rangle_{\text{ens}}$ by:

$$\langle Z(\phi)\rangle_{\text{ens}} = \frac{\int_0^\infty Z g(\Gamma,\phi) e^{-\alpha\Gamma} \mathrm{d}\Gamma}{\int_0^\infty g(\Gamma,\phi) e^{-\alpha\Gamma} \mathrm{d}\Gamma} = \frac{\sum Z e^{-\alpha\Gamma}}{\sum e^{-\alpha\Gamma}}, \tag{3.17}$$

the average force $\langle \overline{F}\rangle_{\text{ens}}$ by:

$$\langle \overline{F}(\phi)\rangle_{\text{ens}} = \frac{\int_0^\infty \overline{F} g(\Gamma,\phi) e^{-\alpha\Gamma} \mathrm{d}\Gamma}{\int_0^\infty g(\Gamma,\phi) e^{-\alpha\Gamma} \mathrm{d}\Gamma} = \frac{\sum \overline{F} e^{-\alpha\Gamma}}{\sum e^{-\alpha\Gamma}}, \tag{3.18}$$

where $\overline{F}$ is the average force for each ensemble packing and the force distribution

$P_{\text{ens}}(F/\overline{F})$ by:

$$P_{\text{ens}}(F/\overline{F}) = \frac{\int_0^\infty P(F/\overline{F}) g(\Gamma,\phi) e^{-\alpha\Gamma} \mathrm{d}\Gamma}{\int_0^\infty g(\Gamma,\phi) e^{-\alpha\Gamma} \mathrm{d}\Gamma} = \frac{\sum P(F/\overline{F}) e^{-\alpha\Gamma}}{\sum e^{-\alpha\Gamma}}. \tag{3.19}$$

Equations (3.17)–(3.20) are then compared with the dynamical measures for a test of ergodicity in Fig. 3.3 in the main text.

3.3.5 Force distribution calculation

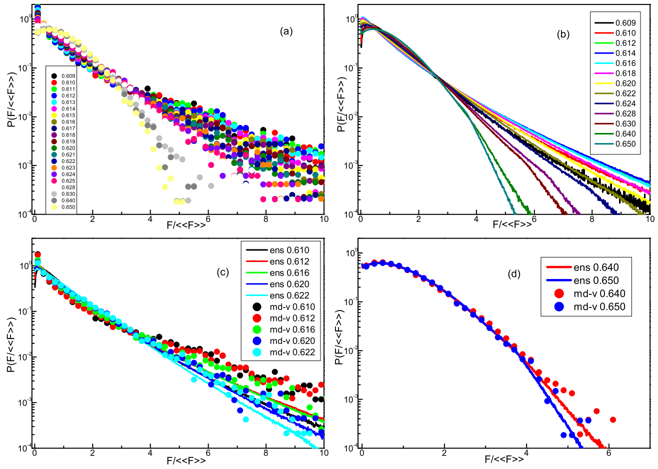

Figure 3.17: (a) The distribution of force $P(F/\langle\overline{F}\rangle_{\text{vMD}})_{\text{vMD}}$, (b) The distribution of force $P(F/\langle\overline{F}\rangle_{\text{ens}})_{\text{ens}}$, (c),(d) The comparison of selected $P(F/\langle\overline{F}\rangle)$ between vMD and ensemble predicted by angoricity.

The distribution of force $\langle P(F/\overline{F})\rangle_{\text{ens}}$ can be calculated by:

$$\langle P(F/\overline{F})\rangle_{\text{ens}} = \frac{\int_0^\infty P(F/\overline{F}) g(\Gamma,\phi) e^{-\alpha\Gamma} \mathrm{d}\Gamma}{\int_0^\infty g(\Gamma,\phi) e^{-\alpha\Gamma} \mathrm{d}\Gamma} = \frac{\sum P(F/\overline{F}) e^{-\alpha\Gamma}}{\sum e^{-\alpha\Gamma}}, \tag{3.20}$$

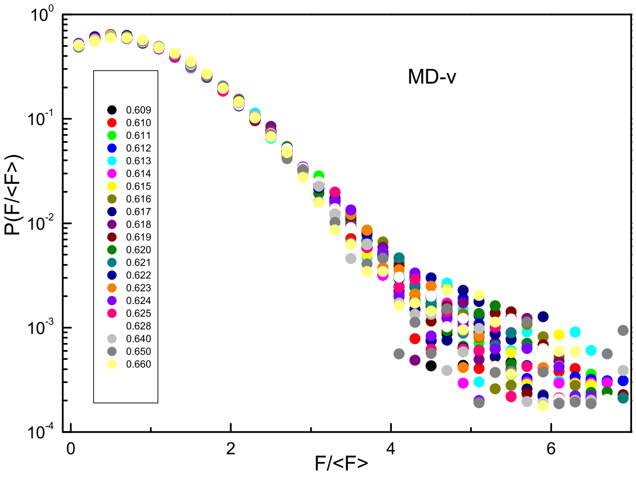

Figure 3.18: The distribution of force $P(F/\langle F\rangle)_{\mathrm{vMD}}$

Since the MD simulations used in the main text are at a predetermined pressure p, there is no difference between the force distribution, $P(F/\overline{F})$ and $P(F/\langle\overline{F}\rangle)$. Here, we use another kind of MD system, with a predetermined volume fraction ϕ, which is not as accurate as the predetermined pressure system used in main text, to obtain the difference between $P(F/\overline{F})$ and $P(F/\langle\overline{F}\rangle)$. The MD simulation is the same, but now, we generate packings at the prefixed volume fraction instead of pressure.

For each system with fixed volume fraction ϕ, the packings can have various pressure. This suggests the force distribution for each packings scaled by the average force over all packings, $P(F/\langle\overline{F}\rangle)$, should be different from the force distribution scaled by that particular packings average force, $P(F/\overline{F})$.

The force distribution for predetermined volume fraction MD simulation(vMD) $\langle P(F/\langle\overline{F}\rangle_{\mathrm{dyn}})\rangle_{\mathrm{dyn}}$ is shown in Fig. 3.17(a). From Fig. 3.17(a), we can find that the force distribution $\langle P(F/\langle\overline{F}\rangle_{\rm dyn})\rangle_{\rm dyn}$ as a function of different volume fraction ϕ no longer collapse. At ϕ close to ϕ_c, the average system force $\overline{F}$ for each packing changes dramatically. While at ϕ is much above ϕ_c, the fluctuation of the average system force $\overline{F}$ decrease, then the force distribution $\langle P(F/\langle\overline{F}\rangle_{\rm dyn})\rangle_{\rm dyn}$ changes continuous.

We can also calculate the force distribution $\langle P(F/\langle\overline{F}\rangle_{\rm ens})\rangle_{\rm ens}$ by the ensemble.

$$\langle P(F/\langle\overline{F}\rangle_{\rm ens}\rangle_{\rm ens} = \frac{\int_0^\infty P(F/\langle\overline{F}\rangle_{\rm ens})g(\Gamma,\phi)e^{-\alpha\Gamma}{\rm d}\Gamma}{\int_0^\infty g(\Gamma,\phi)e^{-\alpha\Gamma}{\rm d}\Gamma}, \tag{3.21}$$

where $\langle\overline{F}\rangle_{\rm ens}$ is the over all average $\overline{F}$ of the ensemble:

$$\langle\overline{F}\rangle_{\rm ens} = \frac{\int_0^\infty \overline{F}g(\Gamma,\phi)e^{-\alpha\Gamma}{\rm d}\Gamma}{\int_0^\infty g(\Gamma,\phi)e^{-\alpha\Gamma}{\rm d}\Gamma}, \tag{3.22}$$

From Fig. 3.17(b), we find the same tendency as obtained from in MD simulation.

Further we check the distribution of force $P(F/\langle F\rangle)$ for our vMD system(see Fig. 3.18). We see that $P(F/\langle F\rangle)$ for different volume fraction ϕ well collapse similar to those obtained from the predetermined pressure system in main text, suggesting that $P(F/\langle F\rangle)$ is a global quantity that can be used to verify if the system is jammed or not.

3.3.6 Entropy Calculation

Here we present the calculation of the "jamming temperature" $T_{\rm J}$ and the corresponding jamming "heat" capacity $C_{\rm J}$. From the power-law relation $p = \Gamma/V \propto (\phi-\phi_c)^a$, we have:

$$\ln p = \ln p_0 + a\ln(\phi-\phi_c), \tag{3.23}$$

where p_0 is the constant depending on the system and the slope $\tan\theta = a$. Figure 3.4 indicates that the jammed system always remain at the positions of maximal entropy $\delta S = 0$ in the direction $(-\sin\theta, \cos\theta)$, perpendicular to the jamming power-law curve. In order to further analyze this result, we plot the entropy distribution along the direction $(-\sin\theta, \cos\theta)$ in Fig. 3.19. We see that the entropy of the corresponding jammed states remains at the peak of the distributions along $(-\sin\theta, \cos\theta)$, verifying the maximum entropy principle in this particular direction. The maximization of entropy is not on Γ or V alone, but on a combination of both. This means that the entropy $S(\ln(\langle\phi\rangle_{\rm dyn} - \phi_c), \ln\langle p\rangle_{\rm dyn})$ is maximum along the direction of $(-\sin\theta, \cos\theta)$ and the slope for the entropy of the jamming power-law curve along this direction $(-\sin\theta, \cos\theta)$ is 0 (see Fig. 3.20), that is,

$$\frac{\partial S}{\partial \ln(\phi - \phi_c)} \sin\theta = \frac{\partial S}{\partial \ln p} \cos\theta. \tag{3.24}$$

Thus we verify the second law of thermodynamics for jammed systems: $\delta S = 0$ at $(\ln(\langle\phi\rangle_{\rm dyn} - \phi_c), \ln\langle p\rangle_{\rm dyn})$.

By the definition of angoricity $A = \partial\Gamma/\partial S$ and compactivity $X = \partial V/\partial S$, we have:

$$\frac{\partial S}{\partial \ln p} = p\frac{\partial S}{\partial p} = \Gamma\frac{\partial S}{\partial \Gamma} = \frac{\Gamma}{A} = \frac{c_1}{A}, \tag{3.25}$$

$$\frac{\partial S}{\partial \ln(\phi - \phi_c)} = (\phi - \phi_c)\frac{\partial S}{\partial \phi} = (\phi - \phi_c)\frac{\partial V}{\partial \phi}\frac{1}{X} = -(\phi - \phi_c)\frac{N V_g}{\phi^2}\frac{1}{X} = -\frac{c_2}{X}, \tag{3.26}$$

where $\phi = N V_g/V$, $c_1 = \Gamma$ and $c_2 = (\phi - \phi_c)(N V_g/\phi^2)$.

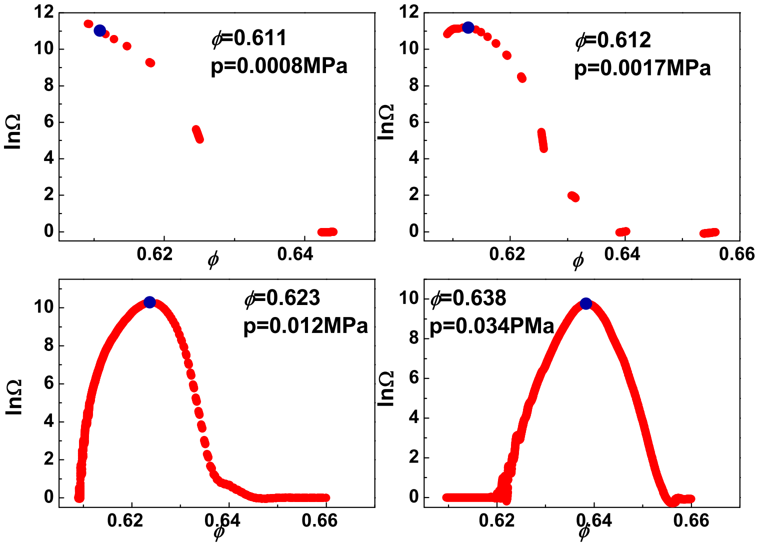

Figure 3.19: The distribution of entropy $S(\ln p, \ln(\phi - \phi_c))$ along the direction $(-\sin\theta, \cos\theta)$ for different jamming ensemble points. The blue ◯ are the entropy for jammed system, which is the maximum of S, verifying the second law of thermodynamics.

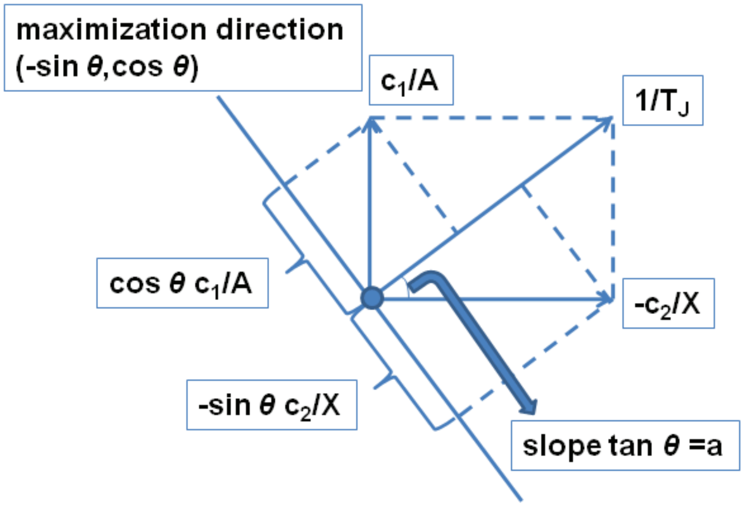

Figure 3.20: The representation of the maximization analysis $\delta S = 0$ along the direction $(-\sin\theta, \cos\theta)$ for one point in the jamming power-law curve. Here $c_1 = \Gamma$ and $c_2 = (\phi - \phi_c)(NV_g/\phi^2)$.

By Eq. (3.25) and Eq. (3.26), we can simplify Eq. (3.24):

$$\frac{c_1}{A} + a\frac{c_2}{X} = 0. \tag{3.27}$$

The relation between X and A can be obtained then:

$$X = -a\frac{c_2}{c_1}A = -a\frac{\phi - \phi_c}{p\phi}A. \tag{3.28}$$

Since we obtain the angoricity $A \propto (\phi - \phi_c)^\gamma$ with $\gamma = 2.5$ in the main text and the pressure $p \propto (\phi - \phi_c)^a$ with $a = 1.5$ (actually we get 1.65 for the small system size used in the main text but the difference can be neglected to simplify). The compactivity $X \propto -(\phi - \phi_c)^2/\phi$. We can therefore define the "jamming temperature" $T_{\rm J}$ as a function of the slope along the direction ($\cos\theta$,$\sin\theta$):

$$\frac{1}{T_{\rm J}} = \frac{c_1}{A}\sin\theta - \frac{c_2}{X}\cos\theta = \cos\theta(a\frac{c_1}{A} - \frac{c_2}{X}) = \frac{c_1}{A\sin\theta} = -\frac{c_2}{X\cos\theta}. \tag{3.29}$$

That is:

$$T_{\rm J} = \frac{A\sin\theta}{c_1} = -\frac{X\cos\theta}{c_2} = \frac{\sin\theta}{\Gamma}A = \frac{a}{\sqrt{1+a^2}}\frac{A}{\Gamma} \sim (\phi - \phi_c)^{\gamma - a} \sim (\phi - \phi_c). \tag{3.30}$$

Furthermore, the "jamming energy" $E_{\rm J}$, corresponding to the "jamming temperature" T_{J} in Eq. (3.29), has the relation as below:

$$\begin{aligned}
\mathrm{d}E_{\mathrm{J}} &= T_{\mathrm{J}}\mathrm{d}S \\
&= T_{\mathrm{J}}\frac{\partial S}{\partial \ln(\phi-\phi_c)}\mathrm{d}\ln(\phi-\phi_c) + T_{\mathrm{J}}\frac{\partial S}{\partial \ln p}\mathrm{d}\ln p \\
&= (-\frac{X\cos\theta}{c_2})(-\frac{c_2}{X})\mathrm{d}\ln(\phi-\phi_c) + \frac{A\sin\theta}{c_1}\frac{c_1}{A}\mathrm{d}\ln p \\
&= \cos\theta\mathrm{d}\ln(\phi-\phi_c) + \sin\theta\mathrm{d}\ln p \\
&= (\cos\theta + \sin\theta\tan\theta)\mathrm{d}\ln(\phi-\phi_c) \\
&= \frac{\mathrm{d}\ln(\phi-\phi_c)}{\cos\theta}.
\end{aligned} \tag{3.31}$$

That is,

$$\mathrm{d}E_{\mathrm{J}} = \sqrt{a^2+1}\mathrm{d}\ln(\phi-\phi_c), \tag{3.32}$$

and

$$E_{\mathrm{J}} = (\sqrt{a^2+1})\ln(\phi-\phi_c). \tag{3.33}$$

The jamming capacity C_{J} can be obtained as:

$$C_{\mathrm{J}} = T_{\mathrm{J}}\frac{\partial S}{\partial T_{\mathrm{J}}} = T_{\mathrm{J}}\frac{\partial S}{\partial \ln p}\frac{\partial \ln p}{\partial T_{\mathrm{J}}} + T_{\mathrm{J}}\frac{\partial S}{\partial \ln(\phi-\phi_c)}\frac{\partial \ln(\phi-\phi_c)}{\partial T_{\mathrm{J}}}, \tag{3.34}$$

Finally, with Eq. (3.24)–(3.26), the capacity C_{J} can be calculated:

$$C_{\mathrm{J}} = T_{\mathrm{J}}(\frac{c_1}{A} - \frac{c_2}{aX})\frac{\partial \ln p}{\partial T_{\mathrm{J}}} = T_{\mathrm{J}}\frac{1+a^2}{a^2}\frac{c_1}{A}\frac{\partial \ln p}{\partial T_{\mathrm{J}}}. \tag{3.35}$$

Since $T_{\mathrm{J}} \sim (\phi-\phi_c)$ and $p \sim (\phi-\phi_c)^{1.5}$, we obtain $C_{\mathrm{J}} \sim (\phi-\phi_c)^{-1}$.

Chapter 4

Potential Energy Landscape Network

We study the energy-landscape network of Lennard-Jones clusters as a model of a glass forming system. We find the stable basins and the first order saddles connecting them, and identify them with the network nodes and links, respectively. We analyze the network properties and model the system's evolution. Using the model, we explore the system's response to varying cooling rates, and reproduce many of the glass transition properties. We also find that the static network structure gives rise to a critical temperature where a percolation transition breaks down the space of configurations into disconnected components. Finally, we discuss the possibility of studying the system mathematically with a trap-model generalized to networks.

4.1 Introduction

In recent years much effort was devoted to the understanding of supercooled liquids and structural glasses, and, in particular, the structural arrest taking place at the glass transition temperature T_g [81, 82]. The numerical investigation of the dynamics of supercooled liquids and glasses is very hard due to the presence, approaching T_g, of this very slow dynamics [32]. An appealing approach for understanding this complex dynamics is to study the properties of the system's "energy landscape": the dynamics of the system is viewed as the motion of the "state point", described by the $3n$-coordinates of all particles in the multi-dimensional configuration space, or landscape, of the potential energy of the system (n is the number of particles). The landscape may be partitioned into "basins of attraction", such that local minimization of the potential energy maps any point in a basin to the same minimum. In recent years it has been shown that the topological details of the basins and the paths connecting them are of great importance in determining the properties of glassy systems (e.g., [83, 84, 85, 86, 87, 88]).

The representation of the landscape by its basins leads to a further simplified view of the energy landscape as a network, where the nodes are the basins and the links are the saddles connecting them. The energy-landscape network of a Lennard-Jones (LJ) system has been mapped, and some of its properties were extracted [23, 89] (for energy-landscape networks in proteins and spin systems see [90, 91, 92]). However, the influence of the topology of the network on the dynamics of the glass transition was never studied. Here, we characterize the networks of mono- and bi-disperse LJ systems obtained by minimization of the potential energy, and use a dynamical model to study properties such as response to cooling. The integration of the landscape picture with network theory provides an interpretation of the different critical temperatures of the glass transition T_0 (Vogel-Tammann-Fulcher temperature [81, 82]) and T_g, as well as identification of a new critical temperature T_p where a second order phase transition separates a phase where a finite fraction of the configurations are available, and a phase with a vanishing number of accessible states.

A network model for the glass transition was introduced in [83, 84]. Here, we take advantage of more sophisticated network analysis tools such as percolation theory. In particular, our approach takes into account the heterogeneity in the number of connections of each basin (i.e., its degree k), which was recently shown to be ubiquitous in nature and crucial for the understanding of many networks' properties [29].

4.2 The Network's Static Properties

We start with a detailed analysis of the static properties of the energy-landscape network. We focus on isolated small LJ systems of two types: *(i)* Monodisperse LJ system (MLJ) with $n = 12, 14$ particles. *(ii)* Binary 80/20 LJ mixture (BLJ) with $n = 8 + 2$ particles. Our network reflects the landscape of potential energy (not free energy), or in other words, the entropy is not taken into account, since we assume that all basins are equivalent in terms of the number of internal states they represent. We note that the sizes of the systems we study are small compared to other systems in which molecular dynamics is run [32]. However, this is inevitable since the number of nodes increases exponentially with the number of particles and thus larger systems are computationally much harder to study [23].

To construct the energy-landscape network, we look for basins, the local minima which form the network's nodes, and their transition states– first order saddles which connect two local minima and form the network's links [23]. We use the LBFGS algorithm [16] to find the basins, and the Eigenvector Following [93] to find the saddles. Sometimes more than one first order saddle connect two linked basins since the landscape is a high dimensional surface. To simplify the network, we consider only the saddle with the minimum energy barrier between two linked basins. While the BLJ system is known to be glassy [32], to avoid the crystallization process usually observed in monodisperse systems, we do not consider the state of lowest energy when setting up the network [84]. Thus, the two systems are expected to be comparable in terms of their glassy behavior.

The MLJ$_{14}$ network consists of $N = 4,193$ nodes and $M = 58,628$ links. The energies at the nodes are distributed approximately normally with mean $\overline{E}(T \to \infty) = -41.5$ (Fig. 4.1(a)). The energy barriers are distributed approximately exponentially $P(\Delta E) = \frac{1}{\overline{\Delta E}} e^{-\Delta E/\overline{\Delta E}}$, where $\overline{\Delta E} = 1.64$ is the average energy barrier (Fig. 4.1(b)). As observed in [23], we confirm that the MLJ$_{14}$ network is *scale-free* [29], i.e. the degree distribution (the probability for a node to have degree k) is broad with a tail decaying as $P(k) \sim k^{-\gamma}$ with $\gamma \approx 2.7$ (Fig. 4.1(c)). The energy of a node decreases with its degree (Fig. 4.1(d)), meaning that the deepest basins can be identified with the network *hubs*, and are thus accessible to/from many other basins. (Interestingly, kinetically constrained models such as facilitated spins [94], show opposite behavior, in which the low energy configurations are in many times frozen and have no access to any other configuraion.) The average barrier height increases with the degree of the node: $\overline{\Delta E} \sim k^{\epsilon}$ with $\epsilon \approx 0.43$ (Fig. 4.1(e)). The average degree of a node's nearest neighbors $\overline{k_{nn}}$ slightly decreases with the node's degree (Fig. 4.1(f)), meaning hubs have many connections to low degree nodes. We also studied "slices" of the network in the degree (using the q-core method [95]) and energy planes. In both cases, we found that removing nodes of low degree, or high potential energy, leaves the network connected.

The MLJ$_{12}$ system is smaller and contains only $N = 508$ nodes and $M = 5,407$ links, leading to larger fluctuations in its statistics. Yet the properties of MLJ$_{12}$ are qualitatively similar to MLJ$_{14}$. For MLJ$_{12}$ we find $\overline{E}(T \to \infty) = -33.87$, $\overline{\Delta E} = 1.16$, $\gamma \approx 3.1$, and $\epsilon \approx 0.41$ (Fig. 4.1). All the results reported henceforth as MLJ are for the MLJ$_{14}$ system, unless explicitly otherwise specified. This picture holds true also for the BLJ network, with $N = 613$ nodes and $M = 6,150$ links. In the BLJ network we obtain $\overline{E}(T \to \infty) = -30.5$, $\overline{\Delta E} = 1.86$, $\gamma \approx 3.4$, and $\epsilon \approx 0.54$ (Fig. 4.1).

4.3 The Network Dynamics

Next we turn to a characterization of the dynamics of the system. We show that application of simple assumptions about the dynamics reproduces many features of the glass transition. At high temperatures, kinetic energy permits access to most states, while for low temperatures, mutual access among basins becomes subject to considerable activation. In low temperatures near the transition (more precisely, below the so-called dynamic glass transition temperature T_d, where an exponential number of meta-stable states appears [82]), the dynamics is dominated

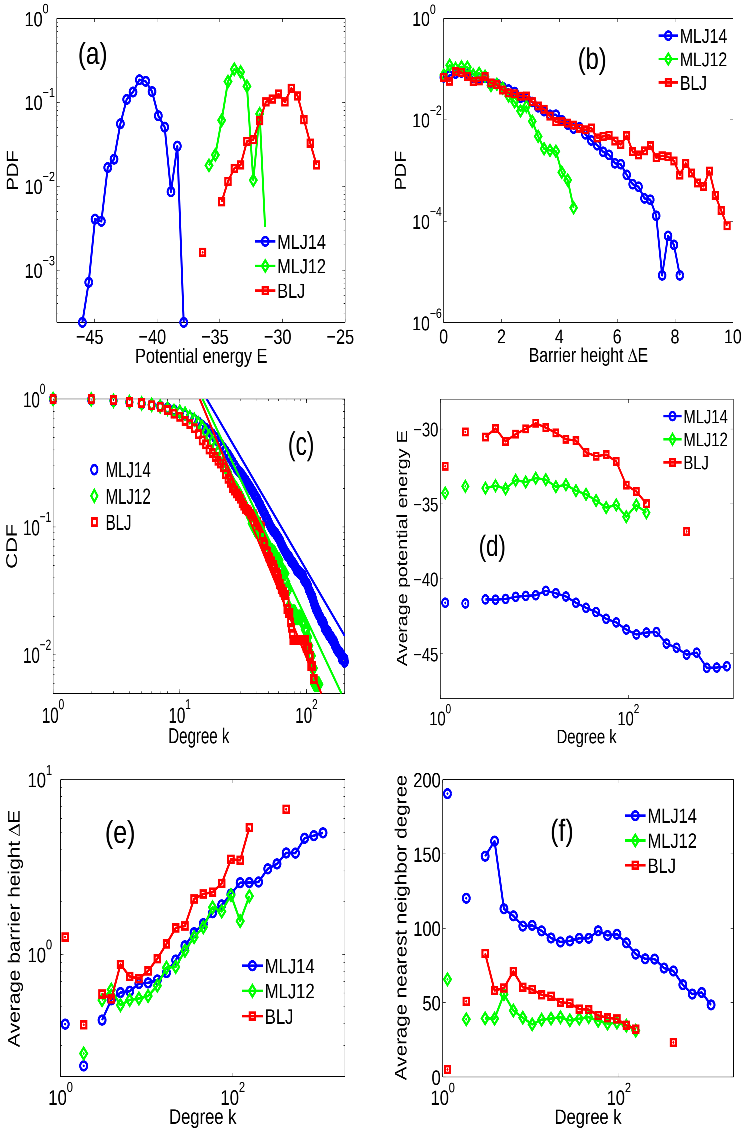

Figure 4.1: Properties of the Lennard-Jones energy-landscape network. Shown are results for MLJ$_{14}$, MLJ$_{12}$, and BLJ (see text). In all figures the data was binned and the average is plotted. (a) Distribution of potential energies E of the nodes. (b) Distribution of the heights of the energy barriers ΔE associated with the network links. (c) Cumulative distribution of node degrees k. Straight lines represent power-law decays of the form $P(k) \sim k^{-\gamma}$, with $\gamma = 2.7, 3.1, 3.4$ for MLJ$_{14}$, MLJ$_{12}$, and BLJ, respectively. (d) The average potential energy of a node E vs. the degree k. (e) The average energy barrier to escape from a node ΔE vs. the node degree k. (f) The average degree of node neighbors $\overline{k_{nn}}$ vs. the node's degree k.

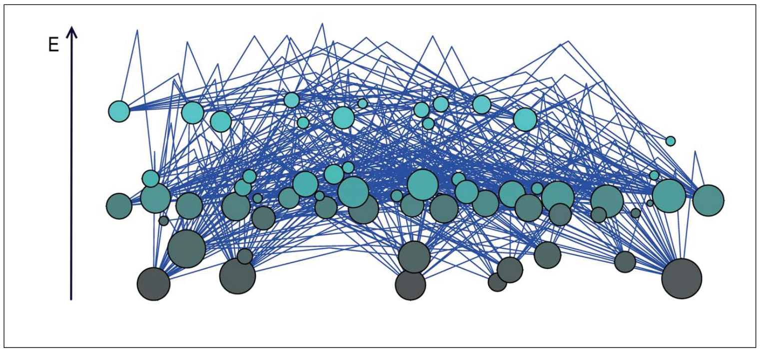

Figure 4.2: MLJ_{10} network schematic. The vertical axis represents the energy, such that nodes with deeper energy are lower (and darker) in the schematic. Links' cusps correspond to the energies of the saddles, and nodes' sizes are proportional to their degree. It can be seen that highly connected nodes usually correspond to deeper basins.

by rare events of collective jumps among different stable positions involving many atoms. Thus, for low temperatures, we neglect the short time dynamics which is dominated by small vibrations within the basins, and model the dynamics of the system as activated jumps between connected states. We assume the transition rate between a pair of linked states follows Arrhenius law:

$$p_{ij} = \frac{1}{N-1} e^{-\Delta E_{ij}/T}, \tag{4.1}$$

where ΔE_{ij} is the height of the barrier separating i and j (not necessarily equal to ΔE_{ji}) and the $1/(N-1)$ factor guarantees that the rate of leaving i, equals to $\sum_{\text{all links } (i,j)} p_{ij}$ is less than 1 for any node. Note there is considerable probability for the system to remain at the current state. This will turn useful in the characterization of the dynamical slowdown.

Experiments [81, 82] and molecular dynamics simulations [32] show that supercooling below the melting point results in a decrease in the system's energy, up to the temperature of the glass transition T_g. At the transition, the system becomes frozen in a disordered configuration, and the rate of change of energy with respect to temperature decreases abruptly (but continuously) to a value comparable to that of a crystalline solid. We suggest, that this picture, as well as the identification of the glass transition temperature T_g can be reproduced using our simple network dynamics.

$\Phi_i(t)$, the probability of the system to be at state i at time t, evolves according to:

$$\frac{d\Phi_i}{dt} = \frac{1}{N-1} \sum_{\text{all links } (i,j)} \Phi_j e^{-\Delta E_{ji}/T(t)} - \Phi_i e^{-\Delta E_{ij}/T(t)} \tag{4.2}$$

We solve this set of equations numerically by iterating Eq. (4.2) once in every time step for the MLJ and BLJ networks. We use different cooling rates $T(t) = T_i - \lambda t$, where T_i is the initial temperature, and λ is the cooling rate. We then calculate $\overline{E}(T) = \sum_i \Phi_i(T(t))E_i$, where E_i is the energy of node i. For infinitely slow cooling, the system can be assumed to be in equilibrium, such that $\frac{d\Phi_i}{dt}$ vanishes for all i. $\overline{E}(T)$ is calculated by setting the Boltzmann distribution $\Phi_i(T) = e^{-E_i/T}/\mathcal{Z}$, where $\mathcal{Z} = \sum_i e^{-E_i/T}$. The results for BLJ, with $\lambda = 0.01 \times \{1/8, 1/16, ..., 1/512, 0\}$, are plotted in Fig. 4.3(a). Indeed we find that our approach qualitatively reproduces the glass-forming behavior.

We then calculate the heat capacity $c = d\overline{E}/dT$ (Fig. 4.3(b)). We associate the temperature for which the heat capacity is maximal with the glass transition temperature T_g. We note that while this association is plausible, it cannot be made rigorous. As expected [32, 81, 82, 96], T_g decreases as the cooling rate becomes slower, approaching its equilibrium value $T_g^0 = 0.67(\pm 0.01)$ for BLJ (Fig. 4.3(b),

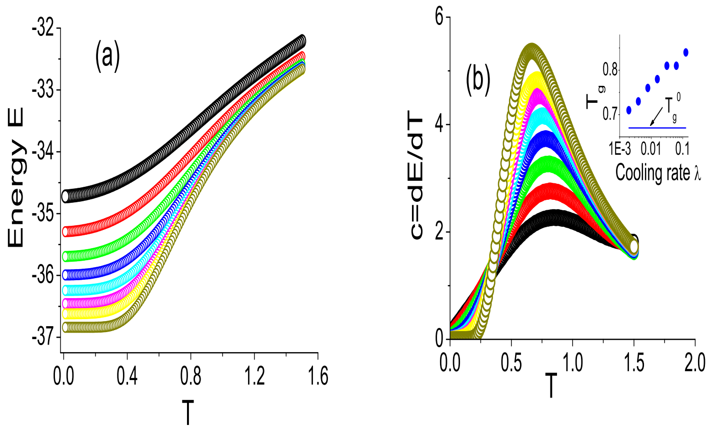

Figure 4.3: (a) Super-cooling in BLJ. The average energy of the system $\overline{E}$ is plotted vs. the temperature $T = T_i - \lambda t$. $T_i = 2$ and the cooling rates are (top to bottom): $\lambda = 0.01 \times \{1/8, 1/16, ..., 1/512, 0\}$, where in each time step we iterate Eq. (4.2) once. Zero cooling rate corresponds to the equilibrium Boltzmann distribution. At $t = 0$ we assumed all states are equally probable. Similar results are found for MLJ (not shown). (b) The heat capacity $c = d\overline{E}/dT$. λ (bottom to top) is same as in (a). Inset: the glass transition temperature T_g as a function of the cooling rate λ. The horizontal line corresponds to T_g^0.

inset). This value of T_g is a little higher than the glass transition temperature in a large BLJ system (≈ 0.45) [32]. For MLJ, the picture is similar with $T_g^0 = 0.47(\pm 0.01)$.

Although in our model, microscopic transition rates follow Arrhenius law, we show below that the global relaxation times deviate from Arrhenius behavior at low temperatures, suggesting that LJ glass forming systems are fragile [81]. A global relaxation time is not naturally defined for the network. However, we note that as the system evolves in time, it explores the phase space in a random fashion, according to the transition probabilities given in Eq. (4.1). Thus, we associate the global relaxation time with the time it takes a random walker with transition

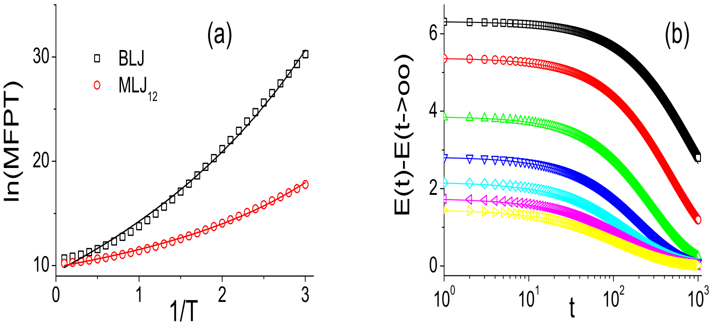

Figure 4.4: Dynamical properties of the energy-landscape network. (a) The mean first passage time (averaged over all sources and destinations) as a function of the inverse temperature $1/T$, for MLJ$_{12}$ and BLJ. A super-Arrhenius behavior is observed (the slope of the curve increases with $1/T$), suggesting that the system is fragile. The lines are fits to Vogel-Tammann-Fulcher law. (b) For several temperatures (top to bottom: $T = \{2.1, 1.8, ..., 0.3\}$), the time evolution of the average energy $\overline{E}(T)$ was calculated. The y-axis shows $\overline{E}(t) - \overline{E}(t \to \infty)$ (symbols), such that all curves approach zero. Curves were fit with a stretched exponential $\overline{E}(t) - \overline{E}(t \to \infty) \propto \exp\left[-(t/\tau)^\beta\right]$ (lines). $\beta \approx 0.8$ and τ is between [50,700], and increasing with $1/T$. The picture is similar for MLJ (not shown).

probabilities as in Eq. (4.1) starting at node i, to arrive to node j (the first passage time [97]), where i and j are randomly chosen, uniformly out of all nodes. (The relaxation time increases with the inverse temperature in a super-Arrhenius form even if the initial sites are weighted by their equilibrium occupation probability $\exp[-E_i/T]$.) Given the network and the energy barrier heights, the average first passage time can be calculated analytically [97]. In Fig. 4.4(a), we plot the mean first passage time (averaged over randomly selected sources and destinations) as a function of the inverse temperature for BLJ and MLJ. A super-Arrhenius behavior is evident, classifying these systems as a fragile glass [81]. The data seem to fit to Vogel-Tammann-Fulcher law $\tau \propto \exp\left[A/(T - T_0)\right]$ with $T_0 \approx 0.1$. However, the precise value of T_0 highly depends on the simulation details.

Time dependent quantities can also be studied with the network. For example, the evolution of the average energy of the system at fixed temperature can be calculated. We use Eq. (4.1) and assume that initially all states are equally probable. The results are presented in Fig. 4.4(b). For short times (up to about 10^3 time steps) the decay fits to a stretched exponential, $\overline{E}(t) - \overline{E}(t \to \infty) = A \exp[-(t/\tau)^{\beta}]$ with $\beta \approx 0.8 < 1$ [82]. For longer times (not shown), the decay is exponential. As in [84], the very fast relaxation, corresponding to transitions within a basin, is not represented in our model.

4.4 Percolation

In addition to dynamical properties, the network topology gives rise to a static critical temperature T_p, where the phase space of configurations breaks into disconnected components. This is revealed by percolation theory applied to the energy-landscape network [98]. Percolation theory is a powerful framework for the study of transport in disordered systems. In its simplest form, it is engaged in the study of conduction in a lattice in which only a fraction p of the sites, or bonds, are conducting [99, 100, 101]. This problem is relevant in various contexts in which critical phenomena take place, from superconductors and gelation to forest fires and oil searching. The theory predicts the value of a critical fraction p_c above which the bulk sample is conducting, as well as the size, dimension, total conductance, diffusion coefficients, and other properties of the percolation clusters.

In recent years, percolation theory has been successfully applied to networks to derive criteria for network stability. In a percolation process over a network,

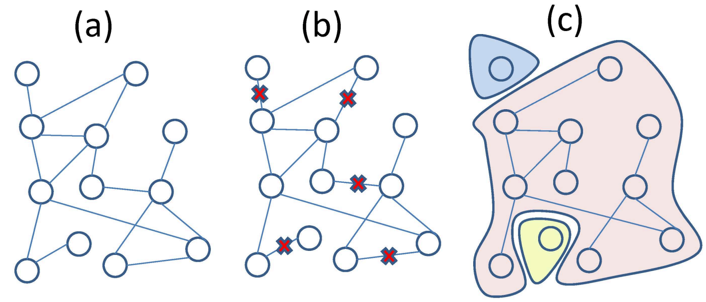

Figure 4.5: A schematic of network percolation. (a) The original network. (b) A fraction $q = 1/3$ (5/15) of the links are removed from the network. (c) The network after removal consists of one large cluster of 10 nodes and 2 small clusters of one node each.

a fraction $q = 1 - p$ of the network links is removed [102, 103]. A percolation transition occurs when a critical fraction $q_c = 1 - p_c$ of the links is removed such that the network disintegrates. The critical point where the network breaks down is identified by a vanishing size of the largest connected cluster as well as a divergence in the size of the second largest cluster [99] (Fig. 4.5).

At least pictorially, the evolution of the connectivity of the energy landscape as the temperature is lowered resembles a percolation process. At high enough temperatures, the system has sufficient thermal energy to cross most energy barriers. Thus, connected basins are accessible from each other and the network is intact. At low temperatures, links which are associated with a barrier of height $\Delta E \gg T$ can practically not be crossed and thus can be considered as absent. Thus, as the temperature is lowered, the network becomes less and less connected, until reaching the percolation threshold where it fully disintegrates. At that point, the system is frozen in an isolated region of the landscape, whose size is a zero fraction of the entire phase space. A percolation transition of the phase space has been predicted long ago for spin glasses [98]. Here, we use the network representation of LJ clusters to show explicitly how the percolation transition is realized.

Since the probability for a link to be "active" decreases with decreasing temperature, we suggest that links are excluded with probability $1 - e^{-\Delta E/T}$, where ΔE is the link's barrier energy. This way, for high T, all links remain and the network is connected, while for low T many links are removed. We then measure (Fig. 4.6) the size of the largest and second largest cluster (where we define a cluster as a set of nodes mutually accessible from each other) for MLJ and BLJ. A percolation transition is evident at $T_p = 0.26 \pm 0.01$ for MLJ and $T_p = 0.47 \pm 0.01$ for BLJ, indicating a second order phase transition between a phase where many configurations are available and a phase with a vanishing number of accessible states.

The percolation transition at T_p is expected to take place at the final stages of the glass transition, when barriers become almost impossible to cross, and the system freezes in the glassy state. Roughly speaking, the percolation transition temperature T_p could be associated with the Kauzmann temperature T_K. At T_K, the configurational entropies of the glass and the crystal are equal (had the glass transition not intervened), and therefore the system is bound to a single, non-crystalline, ideal glass state [81, 82]. Similarly, at T_p, the system is bound to a region of vanishing size of the phase space. In a sense, this region in phase space corresponds to the ideal glass state in which the system is found at the

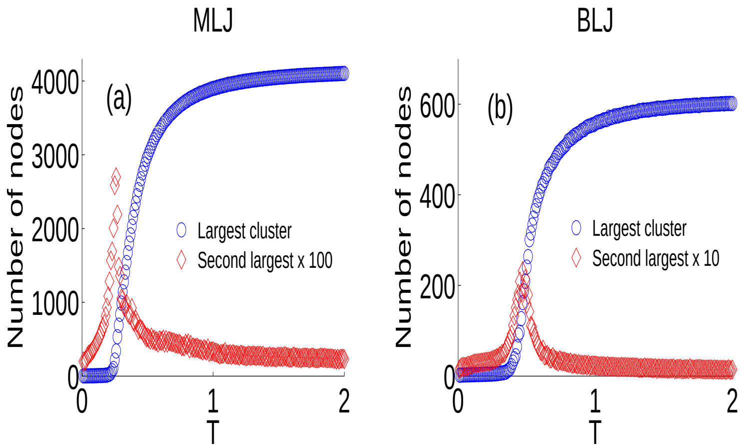

Figure 4.6: Percolation transition in Lennard-Jones energy landscape. (a) For MLJ system, we plot the average size of the largest and second largest cluster after the removal of each link with probability $1 - e^{-\Delta E/T}$. Clusters are strongly connected (i.e., each node can be reached from any other node in the cluster). The percolation transition takes place when the largest cluster size vanishes and the second largest cluster is maximal. (b) Same as (a) for BLJ.

Kauzmann temperature T_K. However we emphasize that this correspondence is merely descriptive and cannot be made more precise.

4.5 Discussion

The understanding of the nature of the glass transition is a formidable task, particularly since molecular dynamics cannot approach low enough temperatures. Thus, simplified models which capture the essential properties of the phenomena are of great value. Representation of the multidimensional energy surface as a network is a particularly appealing approach, due to recently developed network analysis tools. We applied this concept here, where we studied Lennard-Jones clusters as networks of the stable basins and the links connecting them, where each link is associated with an energy barrier. We showed that the network approach qualitatively reproduces many properties of the glass transition. It is still not known whether quantitative information, such as the precise values of T_g and other temperatures can also be extracted from this kind of analysis. For that purpose, larger systems will have to be considered. The similarity, in statistical terms, between the networks of $n = 12$ and $n = 14$ encourages us to believe that similar results, at least qualitatively, will be observed in larger systems.

An alternative approach to circumvent the problem of the small system size is a mathematical model which captures the main properties of the energy-landscape network. A naive attempt would be to construct a "generalized trap model" [104]. In a regular trap model the configurations of the system are fully connected, in the sense that the system can jump from any state to another. However, this is not sufficient to describe the slowing down of the dynamics, since it allows transitions which do not exist in reality [105]. In a trap model adapted to a network, each configuration is linked to precisely k other configurations, where it is particularly interesting to consider the case of a power-law distribution of degrees which is characteristic of LJ (Section 4.2) and other systems [90]. To complete the description of the model, one can assume the distribution of energy barriers is exponential with mean ΔE (Section 4.2). Despite the attractiveness of this simple approach, our analysis shows that it leads to counterintuitive results. For example, the distribution of time τ the system remains in a configuration is a power-law $P(\tau) \sim \tau^{-(1+kT/\Delta E)}$. Thus, according to model, the typical time the system stays at nodes of high degree is small, whereas it expected that the system will spend long time at the hubs, since they are found at low potential energies

(Section 4.2). Therefore, alternative approaches should be sought for.

The advantage of the network approach is manifested in the application of percolation theory, which provides a natural geometrical interpretation of the structural arrest taking place at low temperatures [98]. We studied "bond percolation", where we removed links in which the barrier height was high relative to the temperature, to reveal a critical temperature where the phase space breaks down into small isolated clusters. The study of glassy systems with the network approach can be further extended. For example, ageing phenomena could be studied, for either the real network or the model, by introducing more complex correlation functions. Real-space properties such as diffusion coefficients and fluctuation-dissipation relations could be studied by complementing the network with real-space information for each node. In addition, similar analysis can be pursued to other systems with complex energy landscapes such as proteins (e.g., [106]) or spin glasses [92].

Bibliography

[1] A. Coniglio, A. Fierro, H. J. Herrmann, and M. Nicodemi, *Unifying Concepts in Granular Media and Glasses* (Elsevier, Amsterdam, 2004).

[2] R. P. Behringer and J. T. Jenkins, eds., *Powders & Grains 97* (Balkexma, Rotterdam, 1997).

[3] S. F. Edwards and R. B. S. Oakeshott, *Physica A* **157**, 1080 (1989).

[4] A. J. Liu and S. R. Nagel, *Nature* **396**, 21-22 (1998).

[5] C. S. O'Hern, S. A. Langer, A. J. Liu, and S. R. Nagel, *Phys. Rev. Lett.* **88**, 075507-075510 (2002).

[6] H. A. Makse, D. Johnson, and L. Schwartz, *Phys. Rev. Lett.* **84**, 4160-4163 (2000).

[7] S. F. Edwards, *Physics A* **353**, 114 (2005).

[8] S. F. Edwards and D. V. Grinev, *Phys. Rev. Lett* **82**, 5397-5400 (1999).

[9] R. C. Ball and R. Blumenfeld, *Phys. Rev. Lett.* **88**, 115505 (2002).

[10] S. Henkes and B. Chakraborty, *Phys. Rev. Lett.* **95**, 198002 (2005).

[11] D. J. Wales, *Energy Landscapes*, (Cambridge University Press, Cambridge, 2003).

[12] P. G. Debenedetti and F. H. Stillinger, *Nature* **410**, 259 (2001).

[13] M. Goldstein, *J. Chem. Phys.* **51**, 3728 (1969).

[14] F. H. Stillinger and T. A. Weber, *Science* **225**, 983 (1984).

[15] R. Mari, F. Krzakala and J. Kurchan, *Phys. Rev. Lett.* **103**, 025701 (2009).

[16] D. C. Liu and J. Nocedal, *Mathematical Programming B* **45**, 503-528 (1989).

[17] J. P. K. Doye and D. J. Wales, *J. Chem. Phys.* **116**, 3777 (1994).

[18] C. J. Cerjan and W. H. Miller, *J. Chem. Phys.* **75**, 2800 (1981).

[19] T. S. Grigera, *http://arxiv.org/abs/cond-mat/0509301*.

[20] D. J. Wales and J. P. K. Doye, *J. Chem. Phys.* **119**, 12409 (2003).

[21] D. J. Wales, *J. Chem. Phys.* **101**, 3750 (1994).

[22] D. J. Wales and T. R. Walsh, *J. Chem. Phys.* **105**, 6957 (1996).

[23] J. P. K. Doye, *Phys. Rev. Lett.* **88**, 238701 (2002).

[24] R. Albert, H. Jeong and A. L. Barabási, *Nature* **401**, 130-131 (1999).

[25] S. Milgram, *Psychol. Today* **2**, 60 (1967).

[26] P. Erdös and A. Rényi, *Publ. Math. Inst. Hung. Acad. Sci.* **5**, 17-61 (1960).

[27] B. Bollobás, *Random Graphs* (Academic Press, London, 1985).

[28] D. J. Watts and S. H. Strogatz, *Nature* **393**, 440-442 (1998).

[29] R. Albert and A. L. Barabási, *Rev. Mod. Phys.* **74**, 47 (2002).

[30] H. A. Makse, J. Brujić and S. F. Edwards, *Statistical Mechanics of Jammed Matter*, in H. Hinrichsen and D. E. Wolf, (eds) *The Physics of Granular Media* (Wiley-VCH Verlag, 2004).

[31] F. H. Stillinger and T. A. Weber, *Phys. Rev. A* **25**, 978 (1982).

[32] S. Sastry, P. G. Debenedetti, and F. H. Stillinger, *Nature* **393**, 554 (1998).

[33] W. Kob, F. Sciortino, and P. Tartaglia, *Europhys. Lett.* **49**, 590 (2000).

[34] B. Coluzzi, G. Parisi, and P. Verrocchio, *Phys. Rev. Lett.* **84**, 306 (2000).

[35] A. Fierro, M. Nicodemi, and A. Coniglio, *Europhys. Lett.* **59**, 642 (2002).

[36] L. C. E. Struik, *Physical Aging in Amorphous Polymers and other Materials*, (Elsevier, Houston, 1978)

[37] M. Mézard, G. Parisi and M. A. Virasoro, *Spin Glass Theory and Beyond* (World Scientific, Singapore, 1987).

[38] T. R. Kirkpatrick and D. Thirumalai, *Phys. Rev. B* **36**, 5388 (1987).

[39] T. R. Kirkpatrick and P. Wolynes, *Phys. Rev. A* **35**, 3072 (1987).

[40] L. F. Cugliandolo, J. Kurchan, and L. Peliti, *Phys. Rev. E* **55**, 3898 (1997).

[41] J. Kurchan, Rheology and how to stop aging, in A. Liu and S. R. Nagel, (eds.), *Jamming and Rheology: Constrained Dynamics on Microscopic and Macroscopic Scales*, Taylor & Francis, London, 2001, cond-mat/9812347.

[42] J. Kurchan, *J. Phys. Condensed Matter* **29**, 6611 (2000).

[43] M. Nicodemi, *Phys. Rev. Lett.* **82**, 3734-3737 (1999).

[44] A. Barrat, J. Kurchan, V. Loreto, and M. Sellitto *Phys. Rev. Lett.* **85**, 5034 (2000); *ibid Phys. Rev. E* **63**, 51301 (2001).

[45] H. A. Makse and J. Kurchan, *Nature* **415**, 614 (2002).

[46] S. F. Edwards, The aging of glass forming liquids, in *Disorder in Condensed Matter Physics* (eds J. Blackman, & J. Taguena) 147-154 (Oxford University Press, Oxford, 1991).

[47] S. F. Edwards, The role of entropy in the specification of a powder, in *Granular matter: an interdisciplinary approach* (ed A. Mehta) 121-140 (Springer-Verlag, New York, 1994).

[48] A. Mehta, and S. F. Edwards, *Physica* **A 157**, 1091 (1989).

[49] J. Brujić, S. F. Edwards, and D. Grinev, *Phil. Trans. R. Soc. Lond.* A, **361**, 741 (2003).

[50] E. R. Nowak, J. B. Knight, M. L. Povinelli, H. M. Jaeger and S. R. Nagel. *Powder Technol.* **94**, 79 (1997).

[51] E. R. Nowak, J. B. Knight, E. BenNaim, H. M. Jaeger and S. R. Nagel, *Phys. Rev. E* **57**, 1971 (1998).

[52] P. Philippe, and D. Bideau, *Europhys. Lett.* **60**, 677 (2002).

[53] J. Brujić, P. Wang, C. Song, D. L. Johnson, O. Sindt, and H. A. Makse *Phys. Rev. Lett.* **95**, 128001 (2005).

[54] L. D. Landau and E. M. Lifshitz, *Statistical Physics* (Pergamon, NY, 1970).

[55] T. C. Hales, The Kepler conjecture. *http://arxiv.org/abs/math.MG/9811078.*

[56] J. D. Bernal and J. Mason, *Nature* **188**, 910 (1960);

[57] Anonymous, Nature **239**, 488 (1972).

[58] G. D. Scott, *Nature* **188**, 908 (1960).

[59] J. D. Berryman, *Phys. Rev. A* **27**, 1053-1061 (1983).

[60] G. Y. Onoda, and E. G. Liniger, *Phys. Rev. Lett.* **64**, 2727 (1990).

[61] H. A. Makse, N. Gland, D. L. Johnson and L. M. Schwartz, *Phys. Rev. E* **70** 061302 (2004).

[62] W. G. Ellenbroek, E. Somfai, M. van Hecke and W. van Saarloos, *Phys. Rev. Lett.* **97** 258001 (2006).

[63] S. Henkes, C. S. O'Hern and B. Chakraborty, *Phys. Rev. Lett.* **99** 038002 (2007).

[64] S. Henkes and B. Chakraborty, *Phys. Rev. E* **79** 061301 (2009).

[65] N. Xu, J. Blawzdziewicz J and C. S. O'Hern, *Phys. Rev. E* **71** 061306 (2005).

[66] C. Song, P. Wang and H. A. Makse, *Nature* **453**, 629 (2008).

[67] B. Brujić, S. F. Edwards, I. Hopkinson and H. A. Makse, *Physica A* **327** 201-212 (2003).

[68] L. D. Landau and E. M. Lifshitz *Theory of Elasticity* (Pergamon, NY) (1970).

[69] H. P. Zhang and H. A. Makse, *Phys. Rev. E* **72**, 011301 (2005).

[70] J. H. Snoeijer, T. J. H. Vlugt, M. van Hecke and W. van Saarloos, *Phys. Rev. Lett.* **92**, 054302 (2004).

[71] C. S. O'Hern, S. A. Langer, A. J. Liu and S. R. Nagel SR, *Phys. Rev. Lett.* **86** 111-114 (2001).

[72] M. Wyart, S. R. Nagel and T. A. Witten, *Europhys. Lett.* **72** 486-492 (2005).

[73] G.-J. Gao, J. Blawzdziewicz and C. S. O'Hern, *Phys. Rev. E* **74**, 061304 (2006).

[74] F. Lechenault and K. E. Daniels, *Soft Matter* **6**, 3074 (2010).

[75] B. D. Lubachevsky and F. H. Stillinger, *J. Stat. Phys.* **60**, 561 (1990).

[76] W. S. Jodrey and E. M. Tory, *Phys. Rev. A* **32**, 2347 (1985).

[77] Y. Jin and H. A. Makse, *Physica A* **389**, 5362 (2010).

[78] M. P. Ciamarra and A. Coniglio, *http://arxiv.org/abs/0907.1605*

[79] O. Dauchot, G. Marty and G. Biroli, *Phys. Rev. Lett.* **95** 265701 (2005).

[80] S. Torquato, F. H. Stillinger, *J. Phys. Chem B* **105**, 11849 (2001).

[81] P. G. Debenedetti and F. H. Stillinger, Nature 410, 259 (2001).

[82] W. Kob, *Supercooled Liquids, the Glass Transition, and Computer Simulations* (Springer, 2004).

[83] L. Angelani, G. Parisi, G. Ruocco and G. Viliani, *Phys. Rev. Lett.* **81**, 4648 (1998).

[84] L. Angelani, G. Parisi, G. Ruocco and G. Viliani, *Phys. Rev. E* **61**, 1681 (2000).

[85] L. Angelani, R. DiLeonardo, G. Ruocco, A. Scala and F. Sciortino, *Phys. Rev. Lett.* **85**, 5356 (2000).

[86] S. Buchner and A. Heuer, *Phys. Rev. E* **60**, 6507 (1999).

[87] T. S. Grigera, A. Cavagna, I. Giardina and G. Parisi, *Phys. Rev. Lett.* **88**, 055502 (2002).

[88] B. Doliwa and A. Heuer, *Phys. Rev. E* **67**, 031506 (2003).

[89] J. P. K. Doye and C. P. Massen, *J. Chem. Phys.* **122**, 084105 (2005).

[90] F. Rao and A. Caflisch, *J. Mol. Biol.* **342**, 299 (2004).

[91] E. Ravasz, S. Gnanakaran and Z. Toroczkai, *http://arxiv.org/abs/0705.0912.*

[92] Z. Burda, A. Krzywicki and O. C. Martin, *Phys. Rev. E* **76**, 051107 (2007).

[93] C. J. Tsai and K. D. Jordan, *The Journal of Physical Chemistry* **97**, 11227 (1993).

[94] F. Ritort and P. Sollich, *Advances in Physics* **52**, 219 (2003).

[95] S. Carmi, S. Havlin, S. Kirkpatrick, Y. Shavitt and E. Shir, *Proc. Natl. Acad. Sci. USA* **104**, 11150 (2007).

[96] R. Bruning and K. Samwer, *Phys. Rev. B* **46**, 11318 (1992).

[97] S. Redner, *A Guide to First-Passage Processes*, (Cambridge University Press, Cambridge, 2001)

[98] I. A. Campbell, *Phys. Rev. B* **33**, 3587 (1986).

[99] A. Bunde and S. Havlin, eds., *Fractals and Disordered Systems*, (Springer, New York, 1996).

[100] D. Stauffer and A. Aharony, *Introduction to Percolation Theory*, (Taylor and Francis, London, 1992).

[101] S. Kirkpatrick, *Rev. Mod. Phys.* **45**, 574 (1973).

[102] R. Cohen, K. Erez, D. ben Avraham and S. Havlin, *Phys. Rev. Lett.* **85**, 4626 (2000).

[103] S. N. Dorogovtsev, A. V. Goltsev and J. F. F. Mendes, *Rev. Mod. Phys.* **80**, 1275 (2008).

[104] C. Monthusy and J. P. Bouchaud, *J. Phys. A: Math. Gen.* **29**, 3847 (1996).

[105] Y. Yang and B. Chakraborty, *http://arxiv.org/abs/0810.2484*.

[106] J. Brujić, R. I. Hermans, K. A. Walther and J. M. Fernandez, *Nature Physics* **2**, 282 (2006).